

2 APRIL 1990



**FOREIGN
BROADCAST
INFORMATION
SERVICE**

JPRS Report—

Science & Technology

***USSR: Engineering &
Equipment***

JPRS-UEQ-90-005
2 APRIL 1990

SCIENCE & TECHNOLOGY
USSR: ENGINEERING & EQUIPMENT

CONTENTS

AVIATION AND SPACE TECHNOLOGY

- Gyroscopic Control of Ship Heading
[A. Yu. Panov, Ye. I. Shapkin; SUDOSTROYENIYE, No 9,
Sep 89]..... 1

OPTICS, HIGH ENERGY DEVICES

- Measurement of the Amplitudes and Phases of Surface Acoustic
Waves Using an Automated Laser Installation
[S. S. Sukhanov, G. Garyagdyev, et al.; IZVESTIYA
AKADEMII NAUK TURKMENSKOY SSR: SERIYA FIZIKO-
TEKHNICHESKIKH, KHIMICHESKIKH I GEOLOGICHESKIKH NAUK,
No 6, Nov-Dec 89]..... 9

NON-NUCLEAR ENERGY

- Probabilistic Method for Calculating Higher Harmonic Modes
for an Industrial Electric Power Supply System
[O. T. Geraskin, V. V. Cherepanov, et al.;
IZVESTIYA AKADEMII NAUK LATVIYSKOY SSR: SERIYA
FIZICHESKIKH I TEKHNICHESKIKH NAUK, Nov-Dec 1989].... 13

MECHANICS OF GASES, LIQUIDS AND SOLIDS

- Refinements to a Modified Theory of Anisotropic Plates
[V. A. Rodionova, N. A. Fomina; VESTNIK LENINGRADSKOGO
UNIVERSITETA: MATEMATIKA, MEKHANIKA, ASTRONOMIYA,
Oct 89]..... 21

INDUSTRIAL TECHNOLOGY, PLANNING, PRODUCTIVITY

- An Investigation of Autonomous Low-Frequency Vibration Protection Systems for Ocean Exploration Facilities
[Yu. V. Yakykin, V. A. Gorban, et al.; MASHINODEDENIYE, No 6, Nov-Dec 89]..... 25
- Improving the Characteristics and Increasing the Economy of Automobile Engines by Changing the Phase of Gas Distribution
[M. A. Morozov; IZVESTIYA VYSSHIKH UCHEBNYKH ZAVEDENIY: MASHINOSTROYENIYE, No 1, Jan 90]..... 33
- Thermoanemometric Method of Measuring the Strength of Friction in Reverse Flows
[G. A. Glebov, A. P. Kozlov, et al.; IZVESTIYA VYSSHIKH UCHEBNYKH ZAVEDENIY: MASHINOSTROYENIYE, No 1, Jan 90]..... 39

AVIATION AND SPACE TECHNOLOGY

UDC 629.12.053:681.2.082.16

Gyroscopic Control of Ship Heading

907F0172A Leningrad SUDOSTROYENIYE in Russian No 9, Sep 89 pp 25-26

[Article by A. Yu. Panov and Ye. I. Shapkin]

[Text] The traditional devices for controlling the heading of a ship--rudders and rotary nozzles--have a number of deficiencies, the main ones of which are:

poor controllability and loss of it at low speeds, with no running and in reverse, which results in an increase of the mass and overall dimensions of the rudders and results in installation of steering devices;

large power losses of the ship power plant when ships are moving with transposed rudders (rotary nozzles) due to the occurrence of a longitudinal component of the hydrodynamic force that slows the ship, and up to 40 percent or more of speed is lost in turning [1, 2];

frequent breaks of the rudders and rotary nozzles when moving through clogged and shallow channels and under icing conditions, which results in large losses on repair, related to placing the ship in drydock or a caisson.

The indicated deficiencies are corrected by using gyroscopic devices for controlling the heading of the ship. It is obvious from a patent survey of the problem that studies are being conducted in Great Britain [3], Japan [4], and the USSR [5] on gyroscopic ship control devices. The physical basis of the method of controlling the heading is the capability of a one-axis gyroscope of generating a gyroscopic moment with respect to the hull of the ship. Let a one-axis gyroscope 1

(Figure 1) rotate about the principal axis at angular velocity ω ; the principal axis itself, strengthened in a gimbal 2, rotates at angular

velocity ω_1 . According to the law of mechanics of the moment of momentum, we have:

$$\frac{d\vec{K}_0}{dt} = \vec{u} = m_0 (\vec{F}^e), \quad (1)$$

where K_0 is the moment of momentum of a gyroscope with respect to the center 0, U is the velocity of the end of the vector of the moment of momentum, $m_0(\vec{F}^e)$ is the moment of external forces \vec{F}^e , acting on the gyroscope through the bearings 3.

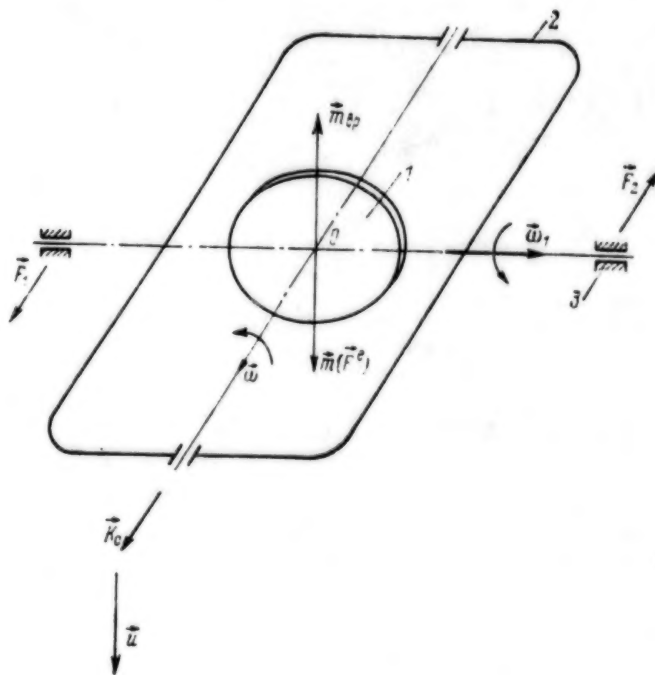


Figure 1. Power Diagram of Gyroscope

The gyroscope in turn acts on the bearing seats 3 with forces F_1 and F_2 , which form a pair with moment m_{bp} . This moment is transmitted to the ship hull, which also causes it to turn along the heading.

Thus, to change the ship's heading, the principal axis of the gyroscope must be rotated about the axis parallel to the main plane of the ship [5]. The resulting gyroscopic moment is calculated by the formula

$$m_{sp} = K_0 \omega_1 \cos \gamma = I \omega_1 \cos \gamma = m R^2 \omega_1 \cos \gamma. \quad (2)$$

where I is the moment of inertia of the gyroscope with respect to the principle axis, m is the mass of the gyroscope, R is its radius and γ is the angle between the principal axis of the gyroscope and the base plane.

An experiment was conducted on the model of a ship to check the theoretical proposition. The specifications of the model of a ship with gyroscope are as follows: length of the hull of $L_M = 1.135$ m, width of the hull of $B_M = 0.196$ m, draft of $T_M = 0.052$ m, mass of $m_M = 6.45$ kg, mass of the gyroscope of $m_g = 0.2$ kg, moment of momentum of $K_0 = 0.392$ kgm^2/s , and rotational frequency of $n_g = 2,250$ rpm. The dependence of the angular rate of turn ω_z and course angle φ of the model on the angular rate of turn (rudder angle) of the principal axis of the gyroscope ω_1 (Figure 2) was found as a result of the tests.

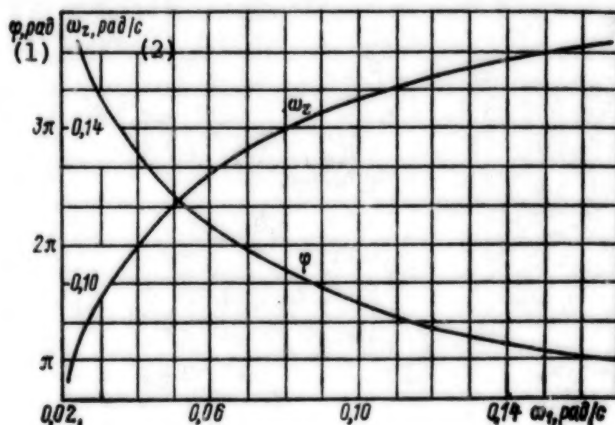


Figure 2. Dependence of Angular Velocity of Ship ω_z and of Course Angle φ on Angular Rate of Transfer of Principle Axis of Gyroscope ω_1

KEY:

1. Radians

2. Radians/s

The technical capability of mounting a heading control gyroscope on various classes of ships was determined from the condition of the equality of moments that turn the ship on the heading, which are created by the control devices and gyroscopes on ships, respectively. The hydrodynamic forces and moments occurring on the rudders and rotary nozzles were calculated by known methods [1, 6].

The gyroscope is selected by the gyroscopic moment m_{Bp} , which guarantees the required controllability to the ship. The rotational frequency of the gyroscope and its radius are determined by the stresses in the rim of the flywheel

$$\sigma = \rho v^2, \quad (3)$$

where v is the circumferential velocity on the rim of the flywheel, m/s, and ρ is the density of the flywheel material, kg/m³.

The stresses σ are limited by the yield point σ_T of the flywheel material. 40KCrNiMo alloy is used as the material [7]. The use of composite flywheels [8] guarantees a reduction of the overall dimensions and weight characteristics of gyroscopes.

The power of the electric motor that rotates the gyroscope is determined from calculation of the frictional losses of the flywheel against air (ventilation losses) and in their bearings. The ventilation losses (kW) for open flywheels are determined by the empirical formula [8]:

$$N_b = (5.7D + 29L) D^4 n^3 \cdot 10^{-5}, \quad (4)$$

where D is the diameter of the flywheel, m, L is the width of the flywheel, m, and n is the rotational frequency, rpm.

These losses are considerable for large-diameter flywheels (they are comparable to the power of the steering devices). However, there are effective methods of reducing ventilation losses: installation of the flywheel in a closed housing, creation of a vacuum in it, or filling it with light gases [9].

The gyroscope is controlled by an electromechanical drive, consisting of an electric motor and reduction gear. Controlling the electric motor, the navigator thus controls the ship. The power of the electric motor of the drive (kW) is determined by the formula

$$N_n = M \dot{\gamma} \eta, \quad (5)$$

where $\dot{\gamma} = \omega_1$ is the angular rotational velocity of the principal axis of the gyroscope, rad/s, η is the efficiency (kN) of the reduction gear, M is the moment on the rotational axis of the gyroscope gimbal, determined by the approximate formula:

Design Parameters of Gyroscopes for Different Classes of Ships

Тип судна	Водонз- мещение, т	Скорость, 1:м/ч	Длина расчетная, м	Осадка, м	{7)Параметры гироскопических средств, создавших такой же момент на корпусе судна		
					(5)	(6) Момент на корпусе судна, созда- емый тра- диционными средствами управления, кН·м	(7)Параметры гироскопических средств, создающих такой же момент на корпусе судна
Сухогрузный теплоход «Якутск»	3325	19,50	105,0	2,510	1066	314,0	1,780
Сухогрузный теплоход типа «Окский-50»	2543	16,80	90,00	2,250	1335	314,0	1,790
Сухогрузный теплоход типа «Ока-1»	1448	14,00	78,00	1,400	200,0	628,0	0,890
Танкер типа «Самотлор»	{14}	1025	15,90	63,70	2,200	361,0	314,0
Самоходная грунтоизычная ша- гапда вместимостью 300 м ³	826,0	12,00	50,60	2,300	96,00	942,0	0,590
Толкач-буксир типа ОТ-2101	{16}	714,3	23,00	44,00	2,140	417,0	314,0
Буксирующий теплоход типа «Улан-Удэ»	{17}	400,0	19,50	38,50	2,030	221,0	314,0
Рейдовый буксирующий теплоход	{18}	251,0	20,50	32,50	2,000	247,0	314,0
							1,780
							2,49
							1,0

(Key on following page)

KEY:

1. Class of ship
2. Displacement, t
3. Speed, km/hr
4. Calculated length, m
5. Draft, m
6. Moment on ship hull, created by traditional control devices, kN·m
7. Parameters of gyroscopes that create same moment on ship hull
8. Rotational frequency of gyroscope, rad/s
9. Radius of gyroscope, m
10. Mass of gyroscope, t
11. Mass of gyroscope in percent of displacement
12. Dry-cargo motor ship of "Yakutsk" class
13. Dry-cargo motor ship of "Okskiy-50" class
14. Dry-cargo motor ship of "Oka-1" class
15. Tanker of "Samotlor" class
16. Self-propelled dirt-hauling barge with capacity of 300 m³
17. Pusher tug of OT-2101 class
18. Tug of "Ulan-Ude" class
19. Harbor tug of BT-861 class

$$M = I_z \omega \dot{\varphi} \cos \gamma, \quad (6)$$

where I_z is the moment of inertia of the gyroscope with respect to the principal axis, $\dot{\varphi}$ is the angular rate of turn of the ship, and γ is the course angle.

The precise formula for determination of moment M is presented in [10]. Calculations by formulas (4)-(6) for an open flywheel D = 0.75 m in diameter and L = 0.46 m wide at rotational frequency of n = 4,500 rpm, which determine the controllability of a motor ship 18 m long, indicate values of $N_B \cong 5$ kW and $N_{II} \cong 2$ kW.

For ships operating in heavy seas, two-flywheel gyroscopes must be used (the calculated mass of the gyroscope is redistributed between the two flywheels). The vectors of the moments of momentum of the gyroscopes in the initial position are established in opposite directions, while linear velocities of the same direction are assigned to their ends. Thus, the harmful lateral gyroscope moments that occur upon rolling of the ship and that have a negative influence on its stability are compensated.

The results of calculating the structural parameters of control gyroscopes are presented in the table. The range of application of control gyroscopes is obvious from the calculations: this is a ship of

displacement up to 2,000 t, operating on rivers with complex channel. The use of these devices on ships of the port and commercial fleet is especially advantageous. The masses of gyroscopes for ships of various classes comprise an average of 0.3-0.7 percent of the mass of the loaded ship, whereas this indicator reaches 0.7-1.0 percent for rudders. It is expected that the mass of control gyroscopes with regard to the mass of the gimbal, substructures and electric motors will be comparable to the mass of existing ship control devices.

In conclusion, we note the main advantages of ship heading control gyroscopes:

they guarantee the required controllability at low speeds, in reverse and in the absence of running speed, where other control devices are hardly effective;

the absence of interaction with the water guarantees high efficiency of these devices, conservation of fuel, and an increase of running speed;

location inside the ship hull guarantees higher reliability and repairability;

ships equipped with gyroscopic control are stable in heading, since the gyroscope spontaneously precesses and generates a moment that holds the ship on course when the ship is affected by perturbing forces.

BIBLIOGRAPHY

1. Voytkunskiy, Ya. I., R. Ya. Pershits, and I. A. Titov, "Spravochnik po teorii korablya. Sudovyye dvizhiteli i upravlyayemost" [Handbook on Ship Theory. Ship Propulsion Devices and Controllability], Leningrad, Izdatelstvo "Sudostroyeniye", 1973.
2. Pavlenko, V. G., "Manevrennyye kachestva rechnykh sudov. Upravlyayemost sudov i sostavov" [The Maneuvering Qualities of River Vessels. The Controllability of Vessels and Barges], Moscow, Izdatelstvo "Transport", 1979.
3. British Patent 1,357,896, MKI V63N 25/08, Improvements in or Relating to a Ship's Steering Device," Ltd. Lithgouss, No 32335/70, Applied for 03 June 71, published 26 June 74, NKI V7U.
4. Tadao, S., Japanese application No. 53-432, MKI V63N 25/00, "Gyroscopic Steering Mechanism," No. 47-29918, Application 25 Mar 72, published 16 Feb 78, NKI 84F3.

5. Panov, A. Yu8. and Yu. L. Panov, "Method of Controlling Ship Heading," Inventor's certificate No. 1244018, OTKRYTIYA, IZOBRETENIYA, PROMYSHLENNYYE OBRAZTSY, TOVARNNYE ZNAKI, No 26, 1986.
6. Sobolev, G. V., "Upravlyayemost korablya i avtomatizatsiya sudovozhdeniya" [The Controllability of a Ship and Automation of Navigation], Leningrad, Izdatelstvo "Sudostroyeniye", 1976.
7. GOST 10994-74. "Splavy pretsizionnye. Marki" [Precision Alloys. Brands], Moscow, Izdatelstvo "Standartov", 1985.
8. Gulina, N. V., "Nakopiteli energii" [Energy Storage Devices], Moscow, Izdatelstvo "Nauka", 1980.
9. Nikitin, Ye. A., S. A. Shestov, and V. A. Matveyev, "Giroskopicheskiye sistemy. Elementy giroskopicheskikh priborov" [Gyroscopic Systems. Elements of Gyroscopes], Moscow, Izdatelstvo "Vysshaya shkola", 1988.
10. Panov, Yu. L. and A. Yu. Panov, "Opredeleniye sil deystvuyushchikh na korpus sudna so storony giroskopicheskogo ustroystva upravleniya kursem" [Determination of the Forces Acting on a Ship Hull by a Heading Control Gyroscope], (deposited at VINITI 18 Sep 87, No. 6771-V87).

UDC 531.7.082.5

Measurement of the Amplitudes and Phases of Surface Acoustic Waves Using an Automated Laser Installation

907F0217 Ashkhabad IZVESTIYA AKADEMII NAUK TURKMENSKOY SSR: SERIYA FIZIKO-TEKHNICHESKIKH, KHIMICHESKIKH I GEOLOGICHESKIKH NAUK in Russian No 6, Nov-Dec 89 pp 79-81

[Article by S. S. Sukhanov, G. Garyagdyyev, K. I. Britsyn, V. G. Grits, K. Nurmukhamedov, V. V. Semenov, E. Ch. Sushinski]

[Text]

Optical sensing methods in current use make it possible to measure the amplitude and phase of surface acoustic waves (SAWs) in various acoustico-electronic devices without disturbing the medium under study. The devices studied include delay lines, band and matched filters, correlators, resonators, etc. One needs to know the parameters of SAWs to monitor physical processes occurring in the material of these products and to improve the characteristics of the products and instruments which are being developed.

Known installations for measuring the parameters of SAWs are bulky and difficult to tune. They are not adapted to work in a wide band of frequencies or to monitor the parameters of products with SAWs during their production [1].

The automated laser installation described below measures the amplitude and phase profiles of SAWs. It is to a great extent devoid of the drawbacks of known installations of this type. Measures taken in the circuitry and construction of this device have made it possible to obtain a high sensitivity to small SAW amplitudes, measurement stability, simplicity of use, and the capacity to work in a wide range of SAW frequencies.

The optical schematic of the installation is shown in Figure 1. The optical quantum generator 1, type LG-38 through a prism with two reflecting surfaces 2 is equipped with a heterodyne channel of the installation with monochromatic radiation ($\lambda_0 = 0.63 \mu\text{m}$); in acoustico-optical modulator 3 (a Bragg cell) there is a spatial and frequency separation of the laser radiation by orders of Bragg diffraction. Two orders of diffraction are used, the zero and the first. The forward ray of the zero order is focused by micro-objective 5 onto the surface of the product under study 6 with SAWs. The reflected ray, which carries information on the amplitude and phase of the SAWs, returns to the acoustico-optical modulator, and diffracting in it, falls on the receiving window of the photodetector 9.

The ray of the quantum generator of the order of diffraction is focused by the micro-objective 8 onto the surface of the mirror 7 and, returning through the

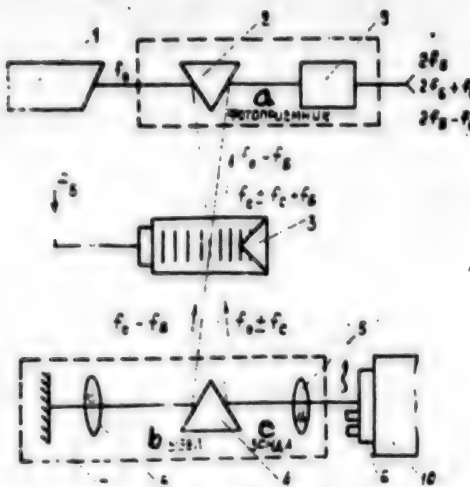


Figure 1. The optical schematic of the installation. a. photoreceiver; b. node; c. sound.

acoustico-optical modulator, also enters the receiving window of the photodetector, forming the heterodyne channel of the installation.

In the photodetector, which is operating in nonlinear mode, there is a transformation of optical signals into radio frequency signals:

$$2f_B, 2f_B - f_c, 2f_B + f_c \quad (1)$$

where f_B is the frequency of the acoustic excitation of the Bragg cell; f_c is the SAW frequency. These signals carry information on the amplitude and phase of SAWs in the product being tested.

Measurement of the phase of SAWs makes significant demands on the stability of the electrical lengths of the measurement and reference channels of the installation. The requirements are considered by equating the optical lengths of the channels after the acoustico-optical modulator, and through construction measures which stabilize and minimize them. At the same time, adjustment mirror 7 provides colinearity of the reference ray in the forward and reverse directions.

Due to the smallness of the diffraction angles in the installation, the division of the rays of the zero and first orders of diffraction is done by a prism with two reflecting surfaces 4. This construction significantly decreases the effect of adjustment error in the reflecting elements on the accuracy of bringing the rays to the receiving window of the photodetector.

The described structure of the optical sensor makes it possible to study SAWs in a wide range of frequencies.

A significant element of the optical system of the installation is the acoustico-optical modulator. At low frequencies a liquid Bragg cell with an excitation frequency of 28 ± 5 MHz is used for this modulator. In terms of construction, the cell is in the form of a cuvette made of a material with significant acoustic absorption. The cuvette is filled with distilled water. A removable piezoelectric transformer is attached to the cuvette in the window with a water-tight seal.

A mode of traveling acoustic waves is provided by choosing a sufficiently long cell and by using a final acoustic absorber. The size of the cell in the direction of the optical beam (L) provides operation in a Bragg diffraction mode:

$$L \geq \frac{2\Lambda^2}{\lambda_0},$$

where Λ is the length of the acoustic wave in the liquid filling the cell and λ_0 is the wavelength of the laser radiation.

In the cell used, $L = 60$ mm, which provides a Bragg diffraction mode at frequencies greater than 10 MHz. At frequencies greater than 60 MHz solid state acoustico-optical modulators are used.

For fine tuning, the cell is placed at an adjustment node. The criterion of optimal adjustment is the maximum of the signal at the output of the photodetector (the adjustment limit is $\pm 0.5'$). There are analogous adjustment nodes at the mirror of the reference channel and at the object stage 10 on which the product to be studied is placed. The linear mechanical sweep of the stage is transformed into an electrical signal which enters input X of the PDS-021 automatic recorder.

Information on the amplitude and phase of SAWs is separated out by processing the signals of the photodetector with an electronic unit, which is a two-channel superheterodyne receiver with a cascade of automatic amplification regulation which is common to both channels. Two signals are processed in the receiving unit (1): $2f_B$ and $2f_B + f_c$. A feature of the schematic is the use of an additional mixer in the second channel to decrease the frequency of the $(2f_B + f_c)$ signal to the frequency of the $2f_B$ signal, as well as the use of the same type of intermediate frequency amplifiers at $2f_B$ in both channels.

The installation uses acoustico-optical modulators at the following frequencies: 28 ± 5 MHz, 80 ± 1 MHz, and 120 ± 3 MHz. Depending on the frequency of the modulator the necessary intermediate frequency amplifiers are installed in the receiving electronic unit. The output signals of the channels are reduced to 465 kHz by reducing mixers and the appropriate heterodynes in the intermediate frequency amplifier complex. These signals enter the input of a standard phasometer, which measures the phase of the SAWs. The signal of the amplitude of the SAWs is the change in the control voltage of the automatic amplification regulation cascade at the input of the receiving electronics unit. The amplitude and phase profiles of the SAWs are recorded in order by an automatic recorder.

Figures 2 and 3 show the amplitude and phase profiles of SAWs measured in a filter with $f_c = 28$ MHz. From the amplitude profile (Figure 2a) and the noise curve (Figure 2b) of the measurement channel one can conclude that the upper curve transmits the deformation of the surface by SAWs of the studied filter with a high degree of accuracy. It is obvious that surface oscillations are grouped toward the longitudinal axis of the product. The phase profile (see Figure 3) makes it possible using known means, to determine the rate of propagation of the SAWs. The described installation is intended for the study of SAW parameters in the range of frequencies from 15 MHz to 300 MHz.

The authors thank A. D. Belyayev for a number of valuable comments expressed during discussion of the work.

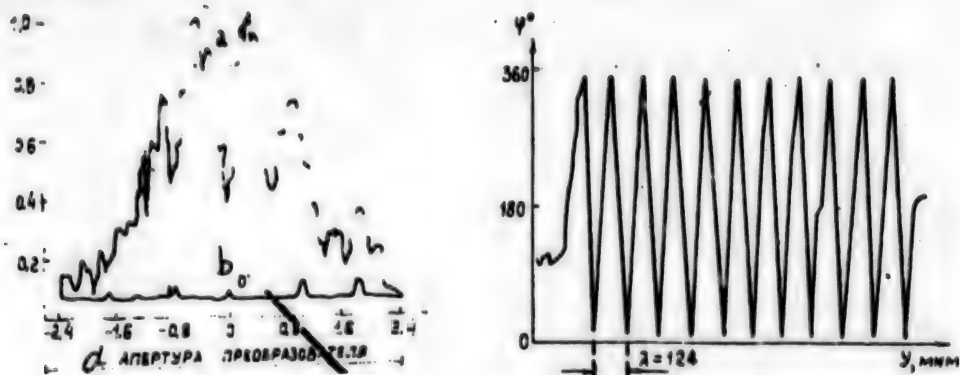


Figure 2 [left]. Amplitude distribution of SAWs in the transverse cross section of the sample (a) and the noise curve (b) of the measurement channel. c. As, relative units; d. aperture of the transformer.

Figure 3 [right]. Distribution of SAW phase in the direction of propagation. X-axis in μm .

BIBLIOGRAPHY

1. De La Rue, R. M., Humphryes, R. F., Mason, I. M., Ash, E. A. Proc IEE 1972 Vol 119 No 2 pp 117-126.

NON-NUCLEAR ENERGY

UDC 621.311:658.562

Probabilistic Method for Calculating Higher Harmonic Modes for an Industrial Electric Power Supply System

907F0174A Riga IZVESTIYA AKADEMII NAUK LATVIYSKOY SSR: SERIYA
FIZICHESKIKH I TEKHNICHESKIKH NAUK in Russian, Nov-Dec 1989 (received 29 Aug
89), pp 112-119

[Article by O.T. Geraskin, All-Union Institute for Advanced Training of Managers and Specialists of USSR Minenergo; V.V. Cherepanov, Kirov Polytechnic Institute; A.V. Rodygin, Izhevsk Agricultural Institute; and G.K. Deksnis, the Physics and Power Engineering Institute of the Lithuanian SSR Academy of Sciences]

[Text] Providing electromagnetic compatibility to electrical power consumers with equipment having nonlinear volt-ampere characteristics and supplying them from the power grid requires the solution of a number of complex problems, including that of calculating non-sinusoidal modes for the electrical supply system¹⁻⁴. The theoretical and experimental studies we have carried out on operating modes for higher-harmonic sources have shown that over long periods of time the higher-harmonic currents they generate vary in a random way due to the stochastic nature of variation in the load over these devices and the voltage of the power grid. The ever-changing configuration of an industrial power grid and changes in the parameters of its elements are also random in nature. In this regard, the development of a probabilistic-statistical method for calculating higher-harmonic modes has significant practical value. In this article we describe a probabilistic method we have developed for calculating the higher-harmonic modes of an industrial power supply system when the mode parameters of its sources vary in a stochastic manner.

Calculating a higher-harmonic mode includes determining the amplitude spectrum of the node voltages and currents in the loops of the supply system equivalent circuit, and the coefficient of higher-harmonic content (non-sinusoidality) of the voltage and equivalent effective higher-harmonic currents in the electrical grid elements. The stochastic nature of variation in the parameters of a higher-harmonic source leads to random variation in these higher-harmonic mode parameters. In this regard, the mathematical model which most adequately describes a non-sinusoidal mode is a probabilistic model. The parameters of the grid elements and their configurations are considered constant and are introduced into the calculation via a determinant operator, while the nonlinear load-induced higher harmonics are modelled with random variables having correlated real and imaginary parts. For the majority of practical problems it is wholly satisfactory to limit oneself to a determination of the numerical probabilistic characteristics of the higher-harmonic mode parameters within the framework of a

correlational theory—one with mathematical expectations, dispersions and correlational moments. A method for numerical calculation of higher-harmonic mode parameter characteristics in terms of the numerical characteristics of the higher-harmonic current source is presented below.

A higher-harmonic mode calculation consists of the following stages:

1. Construct an equivalent circuit for the higher-harmonic power supply system.
2. Calculate the equivalent circuit element resistances at the higher-harmonic frequencies in question.
3. Determine the probabilistic characteristics of the higher-harmonic current generated by devices having nonlinear volt-ampere characteristic curves.
4. Consolidate all higher-harmonic sources connected to the same node of the electrical circuit.
5. Calculate the numerical characteristics of the node voltages and higher-harmonic currents in the loops of the power supply system equivalent circuit.
6. Determine the numerical characteristics of the coefficient of non-sinusoidality of the node voltages and equivalent effective values of the higher-harmonic current in the loops of the equivalent circuit.

The first two stages are performed by a common method used for deterministic calculations of higher-harmonic modes, so we will not look into that in this article.

The third stage includes a calculation, for each ν^{th} harmonic, of the mathematical expectations of the real ($M[J'_\nu]$) and imaginary ($M[J''_\nu]$) components of the random current vector J_ν , the dispersion of J_ν along the coordinate axes $D[J'_\nu]$ and $D[J''_\nu]$, and the correlation coefficient r_{BM_ν} of the real and imaginary components of J_ν . For the canonical harmonics of rectifier converters and thyristor voltage regulators commonly used in industry, these parameters may be calculated by the following formulas:

1. Controllable and noncontrollable rectifiers with a small range of variation in the angle of regulation α (rectifiers for shop dc circuits, converters for ganged dc electric motors, non-reversible converters for electric motors with velocity, voltage or motor emf feedback, etc.):

$$\begin{aligned} M[J'_\nu] &= M[J_\nu] \cos(\gamma M[\psi]); \\ M[J''_\nu] &= M[J_\nu] \sin(\gamma M[\psi]); \\ D[J'_\nu] &= D[J_\nu] \cos^2(\gamma M[\psi]); \\ D[J''_\nu] &= D[J_\nu] \sin^2(\gamma M[\psi]). \end{aligned}$$

For $\nu = 5, 7$:

$$\begin{aligned} r_{BM_\nu} &= +0.5, \quad \text{if } M[J'_\nu]M[J''_\nu] > 0; \\ r_{BM_\nu} &= -0.5, \quad \text{if } M[J'_\nu]M[J''_\nu] < 0. \end{aligned}$$

For $\nu = 11, 13$:

$$r_{BM_\nu} = 0.$$

2. For converters using current stabilizers and three-phase thyristor voltage regulators for metallurgical electric furnaces:

$$\begin{aligned} M[J'_\nu] &= M[J_\nu] \left[1 - \frac{\nu^2}{2} D(\psi) \right] \cos(\nu M[\psi]); \\ M[J''_\nu] &= M[J_\nu] \left[1 - \frac{\gamma^2}{2} D(\psi) \right] \sin(\gamma M[\psi]); \end{aligned}$$

$$D[J'_\nu] = \nu^2 M^2 [J_\nu] D[\psi] \sin^2(\nu M[\psi]);$$

$$D[J''_\nu] = \gamma^2 M^2 [J_\nu] D[\psi] \cos^2(\gamma M[\psi]);$$

$$r_{BM\nu} = -\frac{M^2 [J_\nu] D[J'_\nu] + M^2 [J'_\nu] D[J''_\nu]}{2M[J_\nu] M[J_\nu] \sqrt{D[J'_\nu] D[J''_\nu]}}$$

3. Converters with a large range in variation of the angle of regulation, reversible and non-reversible electric motor converters, converters for plasma steel smelting furnaces, vacuum furnaces, etc.) and three-phase thyristor voltage regulators for deposition-type electric furnaces:

$$M[J'_\nu] = M[J''_\nu] = 0;$$

$$D[J'_\nu] = D[J''_\nu] = \frac{1}{2} M^2 [J_\nu];$$

$$r_{BM\nu} = 0.$$

The parameters $M[J_\nu]$ and $D[J_\nu]$ entering into the formulas are the mathematical expectation and dispersion of the modulus of the ν^{th} harmonic of a converter, and $M[\psi]$ and $D[\psi]$ are the mathematical expectation and dispersion of the angle $\psi = \alpha + \gamma/2$ are defined by the following expressions:

1) for converters with a high range of variation in the angle of regulation,

$$M[J_\nu] = \frac{\sqrt{6} I_{dH}}{\pi \nu} M[I_d^*],$$

where

$$I_d^* = I_d / I_{dH}$$

Here I_{dH} is the nominal rectified current of the converter;

2) for converters with a small range of variation in the angle of regulation,

$$M[J_\nu] = \frac{2\sqrt{6} I_{dH} M[I_d^*]}{\pi \nu^2 M[\gamma]} |\sin(\frac{\nu}{2} M[\gamma])|;$$

$$D[J_\nu] = \frac{6 I_{dH}^2}{\pi^2 \nu^2} D[I_d^*];$$

$$M[\psi] = M[\alpha] + 0.5 M[\gamma];$$

$$D[\psi] = \frac{D[U_d^*]}{1 - M^2[U_d^*]} + D[U_c^*] \cot^2 M[\alpha],$$

where

$$M[\alpha] = \arccos(M[U_d^*] + 0.5 x_k^* M[I_d^*]);$$

$$M[\gamma] = \arccos(\cos M[\alpha] - x_k^* M[I_d^*]) - M[\alpha].$$

Here U_d^* and U_c^* are the relative rectified voltage and the grid voltage, x_k^* is the relative inductive reactance in the commutator circuit of the transformer, and α and γ are the angles of regulation and commutation;

3) for noncontrollable rectifiers

$$M[J_\nu] = \frac{2\sqrt{6} I_{dH} M[I_d^*]}{\pi \nu (\nu - 1) M[\gamma_0]} |\sin(\frac{\nu - 1}{2} M[\gamma_0])|;$$

$$D[J_\nu] = \frac{6 I_{dH}^2}{\pi^2 \nu^2} D[I_d^*];$$

$$M[\psi] = \frac{2}{3} M[\gamma_0],$$

where

$$M[\gamma_0] = \arccos(1 - x_k^* M[I_d^*])$$

4) for three-phase thyristor voltage regulators

$$\begin{aligned} M[J_\nu] &= \frac{0.85}{\nu} I_H; \\ M[\psi] &= 2.7 - 2.1 \frac{M[U_{out}]}{M[U_c]}; \\ D[\psi] &= \frac{4.4}{M^2[U_c]} \left[D[U_{out}] + D[U_c] \frac{M^2[U_{out}]}{M^2[U_c]} \right]. \end{aligned}$$

Here I_H is the regulator load current for $\alpha=0$, and U_{out} is the effective output voltage of the regulator.

Consolidating equivalent higher-harmonic sources is done when several higher-harmonic sources are connected to the same node of an electronic circuit.

The equivalent source should also have a probability characteristic such that, in calculating the harmonic mode parameters, the source mode parameters will be the same before and after consolidating the sources.

A theoretical investigation has shown that the distribution of the equivalent random vector $J_{\nu\Sigma}$ becomes asymptotically closer and closer to a bivariate normal distribution as the number of harmonic sources joined together increases. Its numerical characteristics may be determined from formulas obtained by using the rule for summing independent random vectors:

$$\begin{aligned} M[J_{\nu\Sigma}] &= \sum_{k=1}^n M[J_{\nu k}]; \\ M[J''_{\nu\Sigma}] &= \sum_{k=1}^n M[J''_{\nu k}]; \\ D[J_{\nu\Sigma}] &= \sum_{k=1}^n D[J_{\nu k}]; \\ D[J''_{\nu\Sigma}] &= \sum_{k=1}^n D[J''_{\nu k}]; \\ r_{BM\nu} &= -\frac{M^2[J_\nu]D[J_\nu] + M^2[J''_\nu]D[J''_\nu]}{2M[J_\nu]M[J''_\nu]\sqrt{D[J_\nu]D[J''_\nu]}} \end{aligned}$$

For minimizing the higher-harmonics content, we need to know the probabilistic characteristics of the modulus of $J_{\nu\Sigma}$. Theoretical and experimental studies we have performed showed that the distribution of the modulus of the equivalent current $J_{\nu\Sigma}$ is close to a normal distribution, but with a positive asymmetry that decreases as the correlation coefficient of the components of $J_{\nu\Sigma}$ increases. Decrease in the coefficient of variation in the $J_{\nu\Sigma}$ components also brings the distribution equation for the modulus of $J_{\nu\Sigma}$ closer to normal. So substituting in a normal distribution for the current modulus distribution, we obtain the following expression for determining the mathematical expectation $M[J_{\nu\Sigma}]$ and dispersion $D[J_{\nu\Sigma}]$ of the modulus of $J_{\nu\Sigma}$:

$$M[J_{\nu\Sigma}] = \sqrt{M^2[J_{\nu\Sigma}^2] - 0.5D[J_{\nu\Sigma}^2]}; \quad (1)$$

$$D[J_{\nu\Sigma}] = M[J_{\nu\Sigma}^2] - \sqrt{M^2[J_{\nu\Sigma}^2] - 0.5D[J_{\nu\Sigma}^2]}, \quad (2)$$

where

$$\begin{aligned} M[J_{\nu\Sigma}^2] &= M^2[J'_{\nu\Sigma}] + M^2[J''_{\nu\Sigma}] + D[J'_{\nu\Sigma}] + D[J''_{\nu\Sigma}]; \\ D[J_{\nu\Sigma}^2] &= 4M^2[J'_{\nu\Sigma}]D[J'_{\nu\Sigma}] + 4M^2[J''_{\nu\Sigma}]D[J''_{\nu\Sigma}] + 2D^2[J'_{\nu\Sigma}] + 2D^2[J''_{\nu\Sigma}] + \\ &+ 2r_{B\mu\nu\Sigma}^2 D[J'_{\nu\Sigma}]D[J''_{\nu\Sigma}] + 4M[J'_{\nu\Sigma}]M[J''_{\nu\Sigma}]r_{B\mu\nu\Sigma}\sqrt{D[J'_{\nu\Sigma}]D[J''_{\nu\Sigma}]}. \end{aligned}$$

Formulas (1) and (2) are obtained for the general case in which the components are correlated, dispersion along the axes is not equal, and the mathematical expectation is non-zero. In the particular case of a node being connected to a higher-harmonic source with uniformly distributed phase in the range from 0 to 2π , the numerical characteristics of the equivalent current modulus may be defined in a very simple equation:

$$M[J_{\nu\Sigma}] = \frac{\sqrt{\pi}}{2} \sqrt{\sum_{k=1}^m M^2[J_{\nu k}]}; \quad (3)$$

$$D[J_{\nu\Sigma}] = \frac{4-\pi}{4} \sum_{k=1}^m M^2[J_{\nu k}], \quad (4)$$

which is valid for $m \geq 5$ connected sources. Here the current modulus distribution is subject to the Rayleigh equation. The maximum error in formulas (3) and (4), in comparison to (1) and (2), is no more than 13.5%.

$\dot{U}_{\nu i}$, the voltage of the ν^{th} harmonic at the i^{th} power supply system equivalent circuit node, is a linear combination of the driving currents of the nodes

$$\dot{U}_{\nu i} = \sum_{k=1}^m \dot{Z}_{\nu ik} j_{\nu k}. \quad (5)$$

Here $\dot{Z}_{\nu ik}$ is the complex nodal resistance between the i^{th} and k^{th} nodes, $j_{\nu k}$ is the complex random current from the ν^{th} harmonic of the source connected to the k^{th} circuit node, and m is the number of nodes connected to the harmonic source.

$\dot{U}_{\nu i}$ is completely described by the simultaneous bivariate distributions of a system of random quantities describing its real $U'_{\nu i}$ and imaginary $U''_{\nu i}$ components. Here then

$$\begin{aligned} M[\dot{U}_{\nu i}] &= M[U'_{\nu i}] + jM[U''_{\nu i}]; \\ D[\dot{U}_{\nu i}] &= D[U'_{\nu i}] + jD[U''_{\nu i}]. \end{aligned}$$

Using expression (5) and the theorem about the numerical characteristics, we obtain the following expression for the mathematical expectation and dispersion of the random vector components:

$$M[U'_{\nu i}] = \sum_{k=1}^m R_{\nu ik} M[J'_{\nu k}] + \sum_{k=1}^m X_{\nu ik} M[J''_{\nu k}]; \quad (6)$$

$$M[U''_{\nu i}] = \sum_{k=1}^m X_{\nu ik} M[J'_{\nu k}] + \sum_{k=1}^m R_{\nu ik} M[J''_{\nu k}]; \quad (7)$$

$$D[U'_{vi}] = \sum_{h=1}^m R_{vhk}^2 D[J'_{vh}] + \sum_{h=1}^m X_{vhk}^2 D[J''_{vh}] + \\ + 2 \sum_{h=1}^m R_{vhk} X_{vhk} \sqrt{D[J'_{vh}] D[J''_{vh}]} r_{BMvh}; \quad (8)$$

$$D[U''_{vi}] = \sum_{h=1}^m X_{vhk}^2 D[J'_{vh}] + \sum_{h=1}^m R_{vhk}^2 D[J''_{vh}] + \\ + 2 \sum_{h=1}^m R_{vhk} X_{vhk} \sqrt{D[J'_{vh}] D[J''_{vh}]} r_{BMvh}. \quad (9)$$

Here r_{BMvh} is the correlation coefficient of the real and imaginary components of \dot{J}_{vh} .

For solution of practical problems involving determining the coefficient of non-sinusoidality of the voltage, calculation of damage caused by higher harmonics, and choice of filter parameters, we need to know the numerical characteristics of the random modulus of the voltage of a harmonic at the node $U_{vi} = \sqrt{U'_{vi}^2 + U''_{vi}^2}$, which is completely defined by a univariate distribution. For determining the mathematical expectation and dispersion of the modulus of the voltage of the v^{th} harmonic at the i^{th} circuit node, we obtain the following expression:

$$M[U_{vi}] = \sqrt{M^2[U'_{vi}] + M^2[U''_{vi}] + D[U'_{vi}] + D[U''_{vi}] - D[U_{vi}]} \quad (10)$$

$$D[U_{vi}] = D[U_{vi}] - \Delta^2; \quad (11)$$

$$K[U'_{vi} U''_{vi}] = \sum_{h=1}^m R_{vhk} X_{vhk} (D[J'_{vh}] - D[J''_{vh}]) + \\ + \sum_{h=1}^m (X_{vhk}^2 - R_{vhk}^2) \sqrt{D[J'_{vh}] D[J''_{vh}]} r_{BMvh}. \quad (12)$$

The right-hand side of equation (11) contains two components: $D[U_{vi}]$, the dispersion component obtained by linearizing the function U_{vi} in the neighborhood of the point ($M[U'_{vi}]$; $M[U''_{vi}]$), and Δ^2 , a correction for the nonlinearity of U_{vi} . By virtue of the expression

$$D[U_{vi}] = \\ = \frac{M^2[U'_{vi}] D[U'_{vi}] + M^2[U''_{vi}] D[U''_{vi}] + 2M[U'_{vi}] M[U''_{vi}] K[U'_{vi} U''_{vi}]}{M^2[U'_{vi}] + M^2[U''_{vi}]} \quad (13)$$

$$\Delta^2 = \\ = \frac{\{M^2[U''_{vi}] D[U'_{vi}] + M^2[U'_{vi}] D[U''_{vi}] - 2M[U'_{vi}] M[U''_{vi}] K[U'_{vi} U''_{vi}]\}^2}{4(M^2[U'_{vi}] + M^2[U''_{vi}])^3} \quad (14)$$

The numerical experiment we conducted confirmed the need for the nonlinearity correction Δ^2 . E.g., for $r_{BM}=0$ and the coefficients of variation in the components of the vector \dot{U}_{vi} equal to two, without the correction Δ^2 the error in determining $M[U_{vi}]$ is +15%, and for $D[U_{vi}]$ is -50%.

The harmonics current $\dot{I}_{\nu j}$ in the loops of the equivalent circuit is a linear combination of the driving currents in the nodes:

$$\dot{I}_{\nu j} = \sum_{k=1}^m \dot{C}'_{\nu j k} \dot{J}_{\nu k}. \quad (15)$$

Here $\dot{C}'_{\nu j k} = C'_{\nu j k} + jC''_{\nu j k}$ is the complex coefficient of the current distribution $\dot{J}_{\nu k}$ for the j^{th} loop.

The equations (5) and (15) are identical in structure. Therefore the expressions for determining the mathematical expectation and dispersion of the components of the vector $\dot{I}_{\nu j}$ will be similar to expressions (6) through (9), but instead of real and imaginary components of nodal resistances, we need to insert the real and imaginary parts of the coefficients of the driving current distribution $\dot{C}_{\nu j k}$. The mathematical expectation and dispersion of the modulus of $\dot{I}_{\nu j}$ may be calculated from the formulas (10) through (14), in which instead of the mathematical expectation and dispersion of the components of $\dot{U}_{\nu l}$, we need to insert the mathematical expectation and dispersion of the components of the random vector $\dot{I}_{\nu j}$.

The coefficient of non-sinusoidality of the voltage K_{HC} in the nodes of the supply system is a nonlinear function of the random moduli of the higher-harmonic voltages and the voltage at the fundamental frequency. To a first linear approximation, the mathematical expectation $M[K_{HC}]$ and dispersion $D[K_{HC}]$ may be calculated by the formula

$$M[K_{HC}] = \frac{10^2}{U_H} \sqrt{\sum_{\nu=2}^n M^2[U_{\nu}]} \quad (16)$$

$$D[K_{HC}] = \frac{10^4}{U_H^2} \frac{\sum_{\nu=2}^n M^2[U_{\nu}] D[U_{\nu}]}{\sum_{\nu=2}^n M^2[U_{\nu}]} \quad (17)$$

Here n is the number of higher harmonics, and U_H is the nominal grid voltage.

Using the formulas (16) and (17) is permissible for coefficients of variation in the voltage harmonics of no more than 0.5 and positive correlation coefficients between the voltage harmonics in the nodes.

The error in determining $M[K_{HC}]$ here is no more than 10%. For larger coefficients of variation we need to include a correction for the nonlinearity in the function K_{HC} .

The numerical characteristics of the equivalent effective current in the supply system elements are determined from the equations

$$M[I_e] = \sqrt{\sum_{\nu=1}^n M^2[I_{\nu}];}$$

$$D[I_e] = \frac{\sum_{\nu=1}^n M^2[I_{\nu}] D[I_{\nu}]}{\sum_{\nu=1}^n M^2[I_{\nu}]}.$$

The underlying theoretical hypothesis of this calculation method is confirmed by the results of experimental investigations conducted in ceramics and petrochemical industrial complexes. The deviation between the calculated and experimental higher-harmonic mode parameters is not more than $\pm 30\%$.

- Conclusions.** 1. In this article we have proposed, in solving the question of electromagnetic compatibility, to describe non-sinusoidal mode parameters using random models and systems of random quantities with correlated real and imaginary components. In the majority of cases, determining just the numerical probabilistic characteristics of higher-harmonic mode parameters is enough for solution of most practical problems.
2. A probabilistic-statistical method has been developed for calculating the higher-harmonic modes which enables us to determine the mathematical expectations and dispersions of higher-harmonic voltages in the nodes and harmonic currents in the loops of the supply system equivalent circuit, and the probabilistic numerical characteristics of non-sinusoidality coefficient of the voltages and the equivalent effective currents.

References

1. "Problemy elektromagnitnoy sovmestimosti silovykh poluprovodnikovykh preobrazovateley: Tez. doklady III Vsesoyuz. nauch. tekhn. soveshch. 4.1, 2, 3" [Problems of Electromagnetic Compatibility in Semiconductor Power Converters: Reports to the Third All-Union Scientific and Technical Conference. 4.1, 2, 3], Tallinn: Estonian SSR Academy of Sciences, 1986
2. Geraskin O.T., Cherepanov V.V., Deksnis G.K. "Two forms for the mathematical description of higher-harmonic modes in an industrial power supply system and methods for their solution", IZVESTIYA AKADEMII NAUK LATVIYSKOY SSR: SERIYA FIZICHESKIKH I TEKHNICHEСKIKH NAUK, No 3, 1989, pp 87-91
3. Geraskin O.T., Cherepanov V.V., "Primeniye vychislitelnoy tekhniki dlya rascheta vysshikh garmonik v elektricheskikh setyakh" [Use of Computer Technology for Calculating Higher-Harmonic Modes in Electric Power Grids], Moscow, VIPKenergo, 1987, 53 pages
4. Podygin A.V., Cherepanov V.V. "Oprudeleniye integralnykh kharakteristik modulya toka ekvivalentnogo istochnika vysshikh garmonik pri analize nesinsoidalnykh rezhimov sistem elektrosnabzheniya promyshlennyykh predpriyatiy" [Determining the Integral Characteristics of the Modulus of the Current From Equivalent Higher-Harmonic Sources in the Analysis of Non-Sinusoidal Modes in the Electrical Supply Systems of Industrial Enterprises], Kirov, KirPI, 1988, 9 pages. On deposit at Informenergo, No 2888-En 88.

MECHANICS OF GASES, LIQUIDS AND SOLIDS

UDC 539.3

Refinements to a Modified Theory of Anisotropic Plates

907F0175A Leningrad VESTNIK LENINGRADSKOGO UNIVERSITETA: MATEMATIKA, MEKHANIKA, ASTRONOMIYA in Russian, Oct 89 (received 5 May 88), pp 71-74

[Article by V.A. Rodionova and N.A. Fomina]

[Text] Plate and shell-type structural elements made of polymer composite materials have become commonly employed in designs over the past few years, and this has led to the need for a theory of anisotropic plates and shells that would take into account the specific characteristics of composite materials, such as their low compliance to shear, and low strain resistance in the direction normal to the coordinate surface.

A (modified) theory of anisotropic plates was constructed in ¹, which may be viewed as a first approximation when solving a boundary problem in a three-dimensional theory of elasticity using the weighted residuals method. When employing this method, static boundary conditions over the faces of the plate and the Saint Venant's condition over the cylindrical side surface of the plate are exactly satisfied. It would be of some interest to construct a second approximation (a refined modified theory) that would in addition take into account certain surface load components, self-compensating over the thickness of the plate, that act on the side surface of the plate. It is the construction of just such a theory that is to be examined in this article.

The proposed theory may be constructed by hypothesis. Below, we will use this very approach for construction of a theory of plates corresponding to a second approximation using the weighted residuals method.

In order to make the situation clear, we will limit ourselves to looking at constant-thickness anisotropic plates in the absence of body forces. A plate will be viewed as a thin anisotropic elastic solid possessing a plane of elastic symmetry. An orthogonal curvilinear coordinate system α_1 , α_2 and z is associated with the midplane of the plate, with the linear coordinate z directed perpendicular to it. The primary direction of elasticity coincides with this linear coordinate.

Static boundary conditions are assigned over the face plane of the plate ($z = \pm h/2$)

$$\sigma_{13}^{\pm} = q_1^{\pm}, \quad \sigma_{23}^{\pm} = q_2^{\pm}, \quad \sigma_{33}^{\pm} = q_3^{\pm} \quad \text{for } z = \pm h/2 \quad (1)$$

(where h is the plate thickness). We introduce the following hypotheses:

—(statistical): The perpendicular tangential strains σ_{13} and σ_{23} and normal strain σ_{33} are distributed over the plate thickness according to polynomial equations that are, respectively, of fourth and fifth order in z , i.e.

$$\begin{aligned}\sigma_{i3} &= \frac{m_i}{h} + \frac{q_i z}{h} + \left(\varphi_i + \psi_i \frac{z}{h} + \gamma_i \frac{z^2}{h^2} \right) \left(1 - \frac{4z^2}{h^2} \right), \quad i = 1, 2; \\ \sigma_{33} &= \frac{m_3}{h} + \frac{q_3 z}{h} + \left(\varphi + \psi \frac{z}{h} + \gamma \frac{z^2}{h^2} + \delta \frac{z^3}{h^3} \right) \left(1 - \frac{4z^2}{h^2} \right); \\ \text{or } \sigma_{i3} &= \sum_{k=0}^4 \sigma_{i3}^{(k)} P_k(\zeta), \quad \sigma_{33} = \sum_{k=0}^5 \sigma_{33}^{(k)} P_k(\zeta), \quad \text{where } \zeta = \frac{2z}{h},\end{aligned}\quad (2)$$

—(kinematic): the tangential u_1 and u_2 and normal u_3 components of the displacement vector are distributed over the plate thickness according to polynomial equations that are, respectively, of fifth and fourth order in z , i.e.

$$\begin{aligned}u_i &= \sum_{s=0}^5 \hat{u}_i^{(s)} z^s, \quad i = 1, 2; \quad u_3 = \sum_{s=0}^4 \hat{u}_3^{(s)} z^s, \\ \text{or } u_i &= \sum_{k=0}^5 u_i^{(k)} P_k(\zeta), \quad u_3 = \sum_{k=0}^4 u_3^{(k)} P_k(\zeta).\end{aligned}\quad (3)$$

In these assumed expressions, $\sigma_{i3}^{(k)}$, $\sigma_{33}^{(k)}$, and $u_i^{(k)}$ are functions of the coordinates α_1 and α_2 , $P_k(\zeta)$ are Legendre polynomials, $q_i = q_i^+ - q_i^-$, and $m_i = (q_i^+ + q_i^-)h/2$.

Integrating expression (2) with weighting by P_0 , P_1 and P_2 with respect to z from $z = -h/2$ to $z = +h/2$, we find that

$$\begin{aligned}\sigma_{i3}^{(0)} &= \frac{Q_i}{h}, \quad \sigma_{i3}^{(1)} = \frac{6R_i}{h^2}, \quad \sigma_{i3}^{(2)} = \frac{5\tilde{Q}_i}{h}, \quad \sigma_{i3}^{(3)} = \frac{q_i}{2} - \frac{6R_i}{h^2}, \quad \sigma_{i3}^{(4)} = \frac{1}{h} (m_i - Q_i - 5\tilde{Q}_i), \\ Q_i &= \int_{-h/2}^{h/2} \sigma_{i3} dz, \quad R_i = \int_{-h/2}^{h/2} \sigma_{i3} z dz, \quad \tilde{Q}_i = \int_{-h/2}^{h/2} \sigma_{i3} P_2 dz.\end{aligned}$$

Introducing the integral quantities

$$T_0 = \int_{-h/2}^{h/2} \sigma_{33} dz, \quad M_0 = \int_{-h/2}^{h/2} \sigma_{33} z dz$$

and using the third equilibrium equation (21.5) from ², into which is substituted equation (2) for the tangential stresses, we find, with consideration of boundary conditions (1), an expression for σ_{33} , where

$$\begin{aligned}\sigma_{33}^{(0)} &= \frac{T_0}{h}, \quad \sigma_{33}^{(1)} = \frac{6M_0}{h^2}, \quad \sigma_{33}^{(2)} = \frac{h}{14A_1 A_2} \left(\frac{\partial A_2 \sigma_{13}^{(3)}}{\partial \alpha_1} + \frac{\partial A_1 \sigma_{23}^{(3)}}{\partial \alpha_2} \right) + \frac{m_3 - T_0}{h}, \\ \sigma_{33}^{(3)} &= \frac{h}{18A_1 A_2} \left(\frac{\partial A_2 \sigma_{13}^{(4)}}{\partial \alpha_1} + \frac{\partial A_1 \sigma_{23}^{(4)}}{\partial \alpha_2} \right) + \frac{q_3}{2} - \frac{6M_0}{h^2}, \quad \sigma_{33}^{(4)} = \frac{m_3 - T_0}{h} - \sigma_{33}^{(2)}, \\ \sigma_{33}^{(5)} &= \frac{q_3}{2} - \frac{6M_0}{h} - \sigma_{33}^{(3)}.\end{aligned}$$

Henceforth we will use the following representations for the stresses and strains:

$$\begin{aligned}\sigma_{ij} &= \sum_{k=0}^5 \sigma_{ij}^{(k)} P_k(\zeta), \quad e_{ij} = \sum_{k=0}^5 e_{ij}^{(k)} P_k(\zeta); \quad i, j = 1, 2; \\ e_{i3} &= \sum_{k=0}^3 e_{i3}^{(k)} P_k(\zeta), \quad e_{33} = \sum_{k=0}^5 e_{33}^{(k)} P_k(\zeta).\end{aligned}$$

By directly integrating with respect to z from $z = -h/2$ to $z = h/2$ with weighting factors P_k , using equations (21.1) from ² we find the dependence between the strain components $e_{ij}^{(k)}$ and the displacements $u_i^{(k)}$. In a similar manner, we find the Hooke's Law relations using expressions (2.5.18) and (2.5.19) from ¹.

In equation (3) there are seventeen unknown functions $u_i^{(k)}$ representing all the components of the stress-strain state of the plate. By using equation (2), obtained by consideration of boundary conditions (1) over the face surface of the plate, we express unknown functions $u_i^{(k)}$ ($i=1, 2; k=4, 5$) and $u_3^{(k)}$ ($k=3, 4$) in terms of the others. Then, instead of seventeen, there are only eleven unknown $u_i^{(k)}$.

We introduce, in accordance with the introduced hypothesis, the following expression for the potential energy of plate deformations

$$V = \frac{h}{2} \iint_S \left[\sum_{i,j=1}^3 \left(\sigma_{ij}^{(0)} e_{ij}^{(0)} + \frac{1}{3} \sigma_{ij}^{(1)} e_{ij}^{(1)} + \frac{1}{5} \sigma_{ij}^{(2)} e_{ij}^{(2)} + \right. \right. \\ \left. \left. + \frac{1}{7} \sigma_{ij}^{(3)} e_{ij}^{(3)} \right) + \frac{1}{9} \sum_{i=1}^2 \sigma_{ii}^{(4)} e_{ii}^{(4)} \right] A_i A_j dz_1 dz_2.$$

We obtain equilibrium equations for the plate elements and the natural boundary conditions using the Lagrange variational equation $\delta V - \delta A = 0$ (in the absence of body forces), in which the work of external surface forces over the corresponding virtual displacements $\delta A = \delta A_+ + \delta A_- + \delta A_0$ is equal to the work of surface forces applied to the upper ($z = h/2$) and lower ($z = -h/2$) face planes of the plate, as well as to the cylindrical side surface S_0 .

One may show³ that the system of partial differential equations we are solving is twenty-second order overall. In this case that system is broken down into two systems of equations of tenth and twelfth order, which describes respectively symmetric and antisymmetric stress-strain states of the plate. On each edge of the plate there are eleven boundary conditions. This question is examined in detail in ³.

Comparison of the results of calculations with this theory for an isotropic cantilever beam with transverse tangential load applied to the free end in a quadratic-law distribution over the beam thickness³ with the results of solution of the appropriate boundary problem in the plane elasticity theory by the method proposed in ^{4, p. 77} indicates that the proposed theory and its basis enables us to find the secondary Saint-Venant edge effect-type stress-strain states corresponding to the first of the two roots of the transcendental equations (r) and (x) in ^{4, p. 78}, i.e. it allows us to take into account the effect of these surface load components, self-compensating over the plate thickness and applied to the side surface of the plate, which vary according to a polynomial of no higher than third order in z .

References

1. Rodionova V.A. "Teoriya tonkikh anizotropnykh obolochek s uchetom poperechnykh sdvigov i obzhatiya" [A Theory of Thin Anisotropic Shells With Consideration of Shear and Compression], Leningrad, 1983

2. Novozhilov V.V. "Teoriya uprugosti" [Theory of Elasticity], Leningrad, 1958
3. Rodionova V.A., Fomina N.A. "Utochnennaya teoriya anizotropnykh plastin sredney tolshchiny" [A Refined Theory of Anisotropic Plates of Average Thickness], deposited in VINITI, No 3249-B88, 27 Apr 88
4. Timoshenko S.P., Goodyear J., "Teoriya uprugosti" [Theory of Elasticity], Moscow, 1975

UDC 534.1

An Investigation of Autonomous Low-Frequency Vibration Protection Systems for Ocean Exploration Facilities

907F0107A Moscow MASHINOVEDENIYE in Russian No 6, Nov-Dec 89 [signed to press 24 Oct 89] pp 84-89

[Article by Yu. V. Yadykin, V. A. Gorban, and V. M. Kolotovich, Kiev]

[Text] /The dynamics of low-frequency vibration protection systems which contain a compensator of imposed force, along with elastic and damping elements, is investigated. Results are given from numerical analysis of several structural layouts of vibration protection systems. It is shown that vibration protection systems built on the proposed principle possess a broader working frequency range of vibration protection./

With the development of ocean exploration facilities, the issue of vibration protection of highly sensitive apparatus against the action of low-frequency vibrational loads generated by the rolling motion of the water is becoming increasingly urgent. Traditional methods of vibration protection involving the use of passive elements (inertial, elastic and dissipative) in many cases prove ineffective [1-3].

Analysis of the amplitude-frequency characteristics of vibration protection systems [3-5] suggests one major conclusion--in order to expand the working frequency range it is necessary to reduce the resonance frequency of the system, which exerts major influence on the lower limit of the working range. This can be achieved by lessening the rigidity of the elastic element or increasing the mass of the body being stabilized, which is not always practicable. The change in rigidity of the elastic element and increase in mass of the stabilized body are limited by the permissible static deformation of the elastic element under the action of the stationary load on the body. For a limited stroke of the elastic element $\delta \leq \Delta = F/C$, the frequency of natural oscillations of the stabilized body will be:

$$\omega_n = \sqrt{C/m} \geq \sqrt{F/m\Delta}$$

and depend on the mass of the body m and the permissible deformation of the elastic element.

It is not difficult to see that the requirements imposed on vibration protection systems are contradictory [6]. On the one hand, the elastic element of such systems should be compliant, in order to achieve a low resonance frequency; on the other hand, it should be quite rigid, in accordance with the

conditions of static equilibrium. This narrows the range of effective use of vibration protection systems.

In the present article, we set forth a principle for design of autonomous systems of low-frequency vibration protection--low-frequency decoupling of both passive (no energy supplied) and active type, based on introducing a stationary force input in the compensator system. We also present results of an investigation of the amplitude-frequency characteristics of low-frequency decoupling for ocean exploration facilities. Introduction of the compensator makes it possible to eliminate the basic engineering conflict of vibration protection systems--significantly reducing the stiffness of the elastic element of the vibration insulator without changing its static range. It is shown that effective low-frequency decoupling has an elastic element of low rigidity. In such case, the length of coupling of the source of perturbation and the body being stabilized is self-regulating, i.e., change occurs without employing automatic control systems as a function of the relative displacements of the source and the body being stabilized.

In the coupling that joins the body to the source of perturbation, let us divide the force F into static F_{st} and dynamic F_d components. The static component F_{st} will be compensated by a force of constant magnitude and direction, independent of the velocity, the acceleration, and the relative position of the body being stabilized, while the influence of the dynamic component F_d on the movement of the body being stabilized will be diminished by altering the length of the coupling.

Among the familiar forces in mechanics, we may identify those which satisfy the requirement of constant magnitude and direction for the feasible movements of the object and the source of the perturbations. Such forces include, for example, the force of gravity, the Archimedean force, the centrifugal, hydrodynamic force of a screw, and so on.

The layout for a passive low-frequency vibration protection system includes the object (body being stabilized) and the source of perturbations, joined together by a low-frequency decoupling, in which a compensator of the imposed force is placed in parallel with a vibration insulator. The amplitude-frequency characteristic of the stabilized body, joined to the source of perturbations, has the same appearance as an object connected to a source of perturbations by an elastic element in the trivial layout [2, 6]. However, the resonance frequency for the system (Fig. 1) is shifted into the region of low frequencies of oscillation, i.e., $p_0^* = \sqrt{C/m} - \sqrt{F_d/m\Delta}$ and tends toward zero at the limit.

As an example of the implementation of the principle of construction of a low-frequency decoupling, let us examine several structural layouts for vibration protection systems of this type.

Figure 1 shows a layout in which the force of buoyancy or gravity is used as the compensating static load. A body of mass m_1 is joined to the source of perturbations across a rocking lever with ideal hinge by means of a flexible nonstretching string, passed across the hinge. At the free end of the string is suspended an auxiliary body (compensator) of mass m_2 . Both bodies are joined to the rocking lever by elastic elements. The system is in static equilibrium. The hinge enables self regulation of the length of the coupling

between the body and the source of perturbations (the length of the segment of the coupling between the auxiliary body and the source). In the case when the stabilized body and the auxiliary body are placed in a liquid, the equation of motion of the system is:

$$m_1 \ddot{x}_1 + R_1 |\dot{x}_1| \dot{x}_1 - C_1 (x_0 - x_1) = m_2 \ddot{x}_2 + R_2 |\dot{x}_2| \dot{x}_2 - C_2 (x_0 - x_2), \quad (1)$$

where $x_1 + x_2 = 2x_0$, $x_0 = h \sin \Omega t$ is the external perturbation; $R_1 = 0.5C_{x1}\rho S_1$, $R_2 = 0.5C_{x2}\rho S_2$; m_1 , m_2 are the masses of the stabilized body and the compensator (auxiliary body), taking into account the added masses of the liquid; R_1 , R_2 are the parameters of hydrodynamic resistance of the body and the compensator; C_1 , C_2 are the rigidities of the elastic elements; C_{x1} , C_{x2} are the coefficients of hydrodynamic resistance; S_1 , S_2 are the cross section areas of the stabilized and auxiliary bodies at the maximum midsection; ρ is the density of the medium.

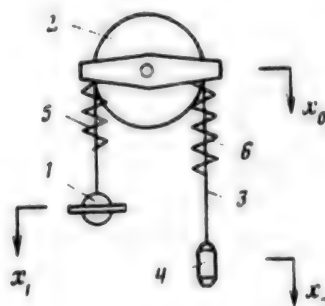


Fig. 1. 1 - body being stabilized, 2 - source of perturbations, a rocking lever with ideal hinge, 3 - flexible nonstretching string, 4 - auxiliary body, 5, 6 - elastic elements.

Using the nondimensional variables:

$$\tau = \Omega t, \xi = x_1/h. \quad (2)$$

we convert equation (1) to the form:

(3)

$$\begin{aligned} \ddot{\xi} + RN|\dot{\xi}|\dot{\xi}/(M+1) + N|2 \cos \tau - \xi|\dot{\xi}/(M+1) + \xi/q^2 &= \\ = 2N|2 \cos \tau - \xi|\cos \tau/(M+1) + [1/q^2 - 2/(M+1)]\sin \tau, \end{aligned}$$

where

$$R = R_1/R_2, \quad M = m_1/m_2, \quad N = \frac{R_1 h}{m_2}, \quad q = \Omega / \sqrt{\frac{C_1 + C_2}{m_1(1+M)}}.$$

Using the above definitions, we find for the tension T of the string:

$$\sigma = \frac{T}{m_1' g} = 1 + \frac{h}{m_1' g} [m_1 \Omega^2 \ddot{\xi} + R_1 h \Omega^2 |\dot{\xi}| \dot{\xi} + C_1 (\ddot{\xi} - \sin \tau)], \quad (4)$$

where $m_1' = m_1 - m_{1B}$ is the mass of liquid displaced by the body being stabilized.

Results of calculations of the dynamic characteristics (amplitude of oscillations ξ_* and maximum tension of the flexible coupling over the period $\sigma_* = T_{\max}/m_1' g$) of the system described by equations (3) and (4) are given in Fig. 2 and 3 by solid lines. The solution of equation (3) is described by the Adams method with zero initial conditions.

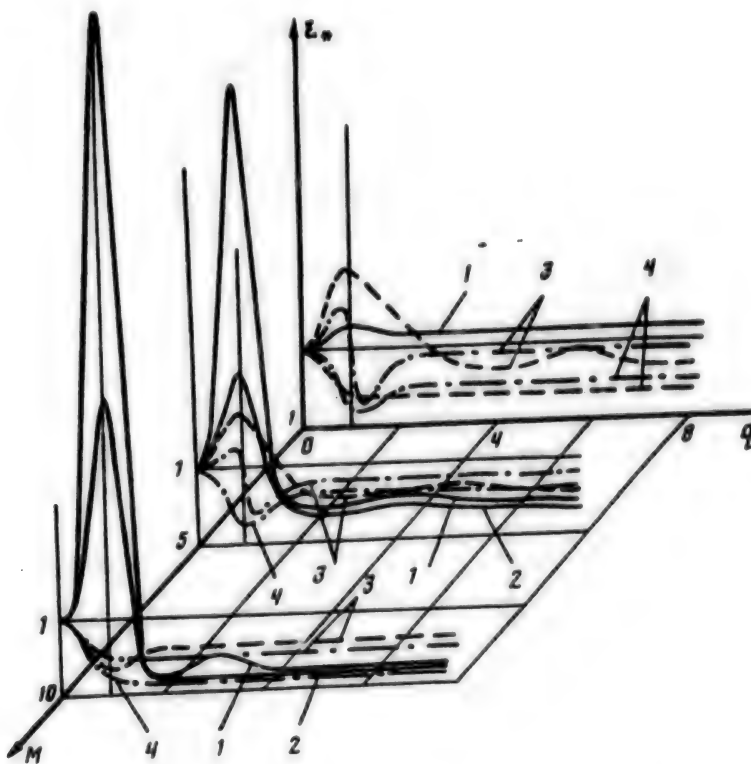


Fig. 2. Amplitude-frequency characteristics of vibration protection systems: 1 - $R = 1$, 2 - 12, 3 - $N = 0.1$, 4 - 10.

As is evident from Fig. 2, with increasing M the amplitude ξ_* of constrained vibrations of the stabilized body decreases. Growth in the parameter M may be achieved by increasing the attached mass of liquid that is placed in motion by the body being stabilized. With increase in the ratio $R = R_1/R_2$, the amplitude of the resonance swings ξ_* diminishes. Increase in parameter R may be achieved by improving the flow around the auxiliary body. Introduction of an elastic coupling ensures that the system is placed in the specified position of static equilibrium with no perturbing force. Lessening the stiffness of the elastic coupling reduces the lower limit of the working frequency range of

vibration protection. The influence of the nonlinearity of the damping on the dynamics of the stabilized body is manifested by appearance of a second resonance swing, the amplitude of which is much less than that of the first resonance swing and diminishes as the parameters R and M increase. The increase in amplitude of the tension T in the flexible string with rise in the relative frequency q (Fig. 3) limits the upper limit of the working frequency region in accordance with the condition $T > 0$ (the flexible coupling only works under tension). Even so, however, the working frequency range of this vibration protection system is broader than that of the familiar ones [3, 4].

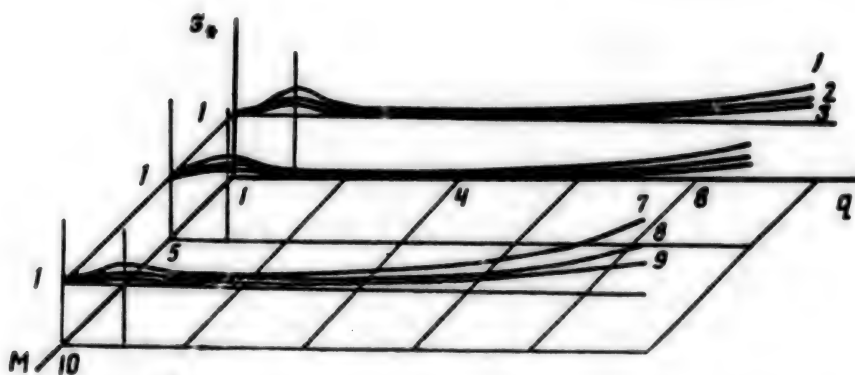


Fig. 3. String tension as function of frequency: 1, 4, 7 - $R = 1$; 2, 5, 8 - 6; 3, 6, 9 - 12.

The case when the compensator (auxiliary body) is located in air ($R_1/R_2 \rightarrow \infty$) is described by equations:

$$\ddot{\xi} + N |\dot{\xi}| \dot{\xi} / (M+1) + \ddot{\xi} / q^2 = [1/q^2 - 2/(M+1)] \sin \tau, \quad (5)$$

$$\sigma = \frac{T}{m_1 g} = 1 + \frac{h}{m_1' g} [m_1 h \Omega^2 \ddot{\xi} + R_1 h^2 \Omega^2 |\dot{\xi}| \dot{\xi} + C_1 h (\ddot{\xi} - \sin \tau)],$$

where $M = m_1'/m_1$, $N = R_1 h/m_1$, $1/q^2 = (C_1 + C_2)/[m_1(M+1)\Omega^2]$.

The results of a numerical analysis of equation (5) are presented in Fig. 2 by the dot and dash lines. The curves of the amplitude of vibrations and the relative tension σ_* against the frequency q are similar to the respective curves for the preceding case. We notice that the dynamic process becomes aperiodic at large values of parameters M and N .

Let us consider a low-frequency decoupling layout (Fig. 4) in which the inertial force of rotation masses is used as compensation. The stabilized body of mass m_1 is placed in liquid and joined by means of a flexible nonstretching string to the piston of a hydraulic cylinder with cross sectional area S_0 , arranged on a movable platform, such as a vessel. The cavities of the cylinder above and below the piston communicate respectively

with the central and peripheral cavities of a hydraulic cylinder of cross section area S_2 , rotating at velocity ω , in which are placed the "compensating" masses m_2 . Both cylinders and the lines which join them are filled with an incompressible fluid. The velocity of rotation is chosen to ensure static equilibrium of the system when the compensators are placed in the middle of their working stroke in the hydraulic cylinder. The piston of area S_0 is connected to the hydraulic cylinder by means of elastic elements. Self regulation of the length of the coupling between the object and the source of perturbations is achieved by changing the position of the piston of area S_0 relative to the hydraulic cylinder in which it is mounted. Rotation of the hydraulic cylinder with the "compensating" masses is accomplished by an external energy source.

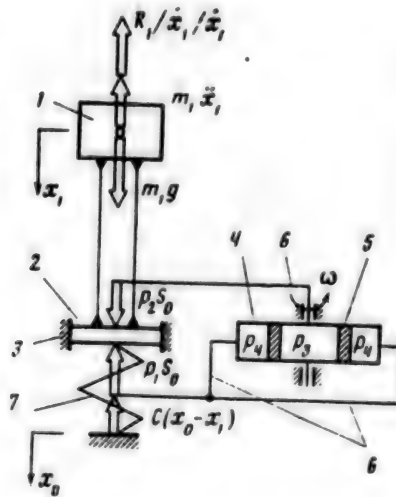


Fig. 4. 1 - stabilized body, 2 - piston, 3 - nonmoving cylinder, 4 - rotating cylinder, 5 - "compensating" masses, 6 - hydraulic lines, 7 - elastic elements.

The equation of force balance for the stabilized body is written as:

$$m_1 \ddot{x}_1 + R_1 |\dot{x}_1| \dot{x}_1 + m_1 g = (p_1 - p_2) S_0 + C(x_0 - x_1), \quad (6)$$

where p_1 and p_2 are the pressure of fluid in the hydraulic cylinder below and above the piston of area S_0 , respectively.

The equation of force balance for the "compensating" bodies is:

$$(p_3 - p_4) S_2 = m_2^* \Delta r - \omega^2 m_2^* (r + \Delta r) + f_1(\Delta r), \quad (7)$$

where m_2^* is the effective mass of the compensating bodies, taking into account the attached mass of fluid; p_3 , p_4 is the pressure of the fluid in the rotating cylinder in its central and peripheral cavities, respectively; r , Δr is the static radius of rotation of the bodies and the dynamic increment in

the radius; $f_1(\Delta\dot{r})$ is a dissipative function, characterizing the resistance to displacement of the bodies in the hydraulic cylinder.

The flow of fluid in the hydraulic lines joining the peripheral cavities of the rotating hydraulic cylinder to the cavity of the nonmoving hydraulic cylinder beneath the piston and the central cavity of the rotating hydraulic cylinder to the cavity of the nonmoving hydraulic cylinder above the piston is described by the Bernoulli equations (not considering the height at which the cross sections are located):

$$\begin{aligned}\frac{p_1}{\gamma} + \frac{(\Delta\dot{r})^2}{2g} &= \frac{p_1}{\gamma} + \frac{(\dot{x}_0 - \dot{x}_1)^2}{2g} + F_1, \\ \frac{p_2}{\gamma} + \frac{(\dot{x}_0 - \dot{x}_1)^2}{2g} &= \frac{p_2}{\gamma} + \frac{(\Delta\dot{r})^2}{2g} + F_2,\end{aligned}\quad (8)$$

where γ is the specific gravity of the fluid; F_1, F_2 are dissipative functions describing the decrease in pressure head in the lines.

The equation of continuity for the fluid in the lines is:

$$\Delta r S_2 = (x_0 - x_1) S_0. \quad (9)$$

From (6) using (7)-(9), we get the equation:

$$m_1 \ddot{x}_1 + R_1 |\dot{x}_1| \dot{x}_1 + C_{x_1} = k^2 m_2 (\ddot{x}_0 - \ddot{x}_1) - k^2 (x_0 - x_1) \omega^2 m_2 + C_{x_0} + F, \quad (10)$$

where $k = S_0/S_2$.

The inertial and dissipative forces of the fluid may be disregarded, since they are small in comparison to the force of hydrodynamic resistance of the body being stabilized, i.e.,

$$\frac{k^2 \omega^2 m_2 (x_0 - x_1)}{R_1 |\dot{x}_1| \dot{x}_1} \ll 1, \quad \frac{F}{R_1 |\dot{x}_1| \dot{x}_1} \ll 1. \quad (11)$$

Using definitions (2) and noting (11), we shall write the equation of vibrations (10) and the expression for the tension of the string in the nondimensional form:

$$\begin{aligned}\ddot{\xi} + N |\dot{\xi}| \dot{\xi} / (M + k^2) + \xi / q^2 &= [1/q^2 - k^2 / (M + k^2)] \sin \tau, \\ \sigma = \frac{T}{m_1' g} &= [m_1' h \Omega^2 \ddot{\xi} + R_1 h^2 \Omega^2 |\dot{\xi}| \dot{\xi} + Ch(\xi - \sin \tau)] / m_1' g + 1.\end{aligned}\quad (12)$$

The results of numerical analysis of equation (12) are given in Fig. 2 by dotted lines.

Thus, the dynamics of the above vibration protection systems is described by a single class of equations, and the results of their analysis are comparable. The investigations demonstrate the possibility of ensuring effective low-frequency decoupling of an object from the low-frequency perturbations caused, for example, by the rolling of the platform of the ocean exploration facilities.

Bibliography

1. Kolovskiy, M. Z., "Avtomatuskoye upravleniye vibrozashchitnymi sistemami [Automatic Control of Vibration Protection Systems]," Nauka, M., 1976, 317 pp.
2. Ganiyev, R. F., Kononenko, V. O., "Kolebaniya tverdykh tel. [Oscillations of Solids]," Nauka, M., 1976, 431 pp.
3. Tikhomirov, Yu. F., "Promyshlennyye vibratsii i borba s nimi [Industrial Vibrations and Their Control]," Tekhnika, Kiev, 1975, 184, pp.
4. "Vibratsii v tekhnike [Vibrations in Machinery]," Vol 3, Mashinostroyeniye, M., 1980, 543 pp.
5. Yablonskiy, A. A., Noreyko, S. S., "Kurs teorii kolebanniy [A Course in the Theory of Oscillations]," Vyssh. shk., M., 1961, 208 pp.
6. Chuprakov, Yu. I., "Gidravlicheskiye sistemy zashchity operatora ot obshchey vibratsii [Hydraulic System for Protecting an Operator Against General Vibration]," Mashinostroyeniye, M., 1987, 224 pp.

UDC 621.434-3

Improving the Characteristics and Increasing the Economy of Automobile Engines by Changing the Phase of Gas Distribution

907F0186a Moscow IZVESTIYA VYSSHIKH UCHEBNYKH ZAVEDENIY:
MASHINOSTROYENIYE in Russian No 1, Jan 90 pp 73-77

[Abstract and Article by M. A. Morozov, graduate student. Abstract consists of the first three paragraphs.]

[Text]

One of the drawbacks of internal combustion automobile engines is that the gas distribution phases do not correspond to their optimal values. To eliminate this, it is desirable to regulate the phases of gas distribution in the process of engine operation.

Most promising is an additional device before the intake valve.

Based on calculations, the requirements have been formulated for a regulating cutout element before the intake valve.

One of the drawbacks of existing automobile engines is the lack of correspondence between the phases of gas distribution, especially the end intake phase, and optimal values. This holds true in the majority of speed and load modes. By shortening the phase one can significantly expand those areas of speed characteristics with a high torque and accommodation coefficient. But at high frequencies of crankshaft rotation the torque and power decrease in comparison to the torque and power reached in a longer end intake phase.

So began the attempt to change the phases of gas distribution during engine operation. However, only the end intake phase and the begin exhaust phase could be varied over a wide range, since their times are not limited by the meeting of the piston with the open valve.

In recent years, as progress in engine characteristics has accelerated, simple designs have been exhausted, and new designs found which were suitable for mass production, it became possible for industry to use devices to implement near optimal phases of gas distribution during engine operation in each speed mode (Alpha-Romeo, Nissan, Honda, Mercedes).

Devices to change the phases of gas distribution can be divided into several groups according to their characteristics. These are devices for stepped and stepless

change in the angular position of the camshaft relative to the crankshaft with mechanical, hydraulic, electrical, or combined control [1].

The simplest of the known devices is a stepless means of changing the angular position of the camshaft relative to the crankshaft. Screw, chain, geared drive, or differential mechanisms or devices are used for this.

The simple design of these devices conflicts with their principal drawback, simultaneous change in the phase of the beginning and end of intake. Practical means of varying the phases in this way do not exceed 30-40° of the rotation of the crankshaft because one must prevent the collision of open valves and pistons. But even such a relatively small change in phases yields positive results: one can increase the filling of cylinders at low rotation frequencies and increase the supply of torque and the power per liter.

A more complex means of stepless regulation of gas distribution phases is based on the use of a camshaft consisting of two mutually joined parts. In each part (the internal and external) are cams whose sides touch. The mechanism controlling the mutual movement of the cams makes it possible to separate them by an angle of up to 44°.

Another design was developed by Fiat. Fiat created a mechanism with cams which were wider than the surface of the push rod sliding along it and with a variable profile along the axis. The regulation was done by shifting the camshaft along the axis. In a means of stepped phase regulation patented by the Matsuda firm, the camshaft has two sets of cams with different profiles (for low and high rotation frequencies). Each valve of the mechanism is comprised of two rockers, one of which has a constant kinematic link with the valve. The other comes into contact by blocking in the transition to a high speed mode.

In a separate group are additional cutout devices in the intake tract which, in addition to regulating phase, decrease the throttle losses which are inherent in engines with quantitative regulation and a rotation which increases sharply as frequency decreases. Volkswagen has used a rotating slide valve (Figure 1) before the intake valve in an experimental engine.

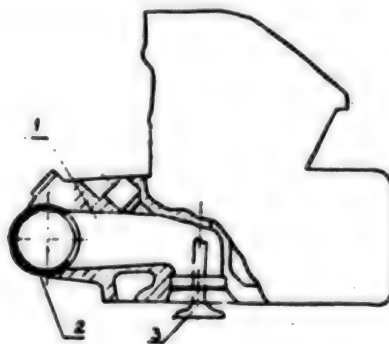


Figure 1. 1. intake channel; 2. rotating slide valve; 3. intake valve.

The slide valve, which is driven by a device which varies its angular position relative to the crankshaft, may cut off the intake channel at any moment (without limit) and change the effective phase of the end of intake by shortening it in

relation to the corresponding phase of the main intake valve. But since the slide valve rotates with a constant angular speed equal to the speed of the main camshaft, its window does not have fixed open and closed positions, which inevitably leads to an increase in throttle losses.

Moreover, the slide valve has a long developed cylindrical surface. If one is to provide a small clearance in the slide valve in relation to the immobile parts in contact with it, this leads to the passage of a live charge through the contact while "advancing" the cutout of the cylinder at the intake manifold.

The use of such a device reveals great possibilities for controlling the actual phase of the end of intake, from delaying it to significantly advancing it in relation to lower dead center. In the latter case, one can sharply decrease the charge of the cylinders without throttling in the carburetor, that is, without creating a significant vacuum in the intake collector. Indeed, the prerequisites for theoretically throttleless quantitative regulation are created. However, practically, due to aerodynamic imperfection of the "broken" line of the intake channel from the carburetor to the valve due to partial mismatching of the axes of circumference in the slide valve and in the nozzle, the throttle losses are partially preserved.

An interesting feature of the ideal process of filling the cylinder in the presence of this type of device is the near adiabatic decrease in the charge temperature when its entrance to the cylinder is closed early (in relation to lower dead center). The closer the additional cutout device to the valve, the higher the degree of cooling. A calculation using a very simple expression of the polytrope when its index is close to 1.4 shows that when the entrance of charge into the cylinder is closed 40° before lower dead center, its temperature decreases by 30°, and when it is closed 45° before lower dead center, temperature decreases by 50°. Such substantial cooling aids an intense decrease in the tendency to detonate, its prevention despite the very early onset of ignition and the low octane number of the fuel. Thus, one can sharply reduce the requirement on the antidentalation properties of benzine without worsening fuel economy in the most characteristic traveling modes. However, the design proposed by Volkswagen is far from ideal.

Let us examine the effect of deviations from the theoretical cycle on energy losses.

1. The presence of a gap in the contact with the cylinder head leads to the entrance of fuel into the cylinder when the slide valve is closed, but when the intake valve is still open. Considering the value of the entrance of fuel in the cylinder through the gap, we get its dependence on the value of the gap (Figure 2, curves 1 and 2). It is clear from the graph that even a small increase in the gap makes the course of the working cycle much worse. As the frequency of rotation of the engine increases, this correlation increases. But due to the great length of the slide valve it is rather difficult to provide a small gap in its contact with the casing.

2. The presence of a "parasite" volume between the slide valve and the intake valve leads to a decrease in the degree of regulation of the engine, which is linked with the difference in the volumes of polytropic expansion in the cycle of intake and subsequent compression. By using the equation of the polytrope we obtain the dependence of the theoretical losses of this type on the "parasite" volume (Figure 3). It follows from these relations that the "parasite" volume must be decreased to about 10% of the cylinder volume.

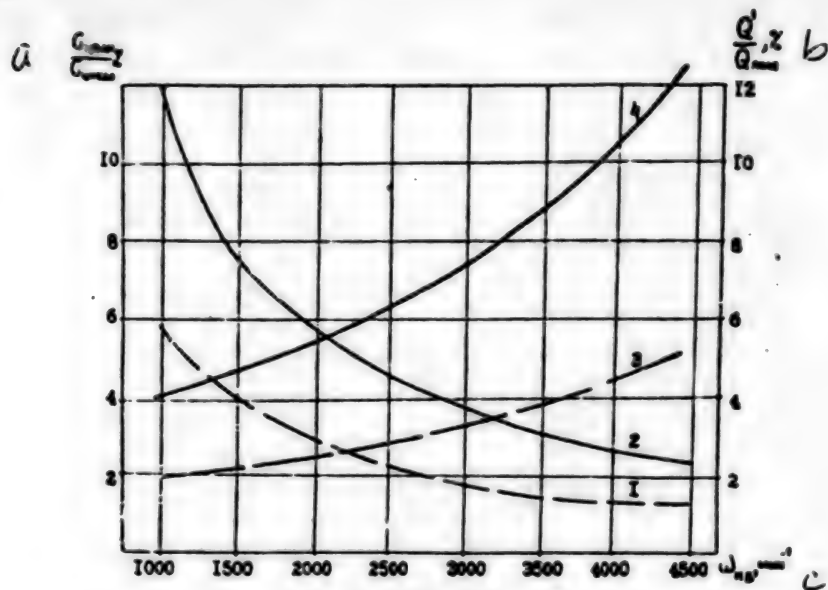


Figure 2. 1. radial gap of 0.05 mm; 2. radial gap of 0.1 mm; closure time of the gate equal to the time for the camshaft to rotate (3) 10°, (4) 20°. a. Q_{gap}/Q_{cyls} %; b. Q'/Q_{fleld} %; c. ω_{nq} , min⁻¹.

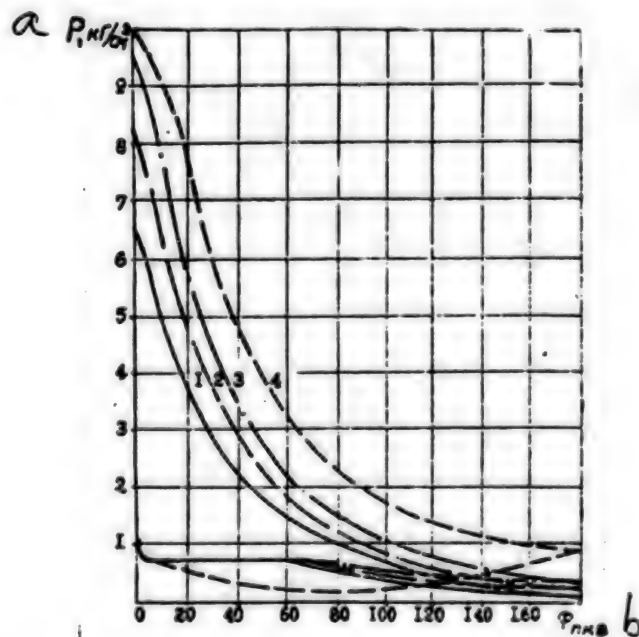


Figure 3. "Parasite" volume composed of the volume of the cylinder; 1, 10; 2, 20; 3, 30; 4 engine without an additional device at the intake. a. P , kg/cm²; b. $\Phi_{rot. crankshaft}$.

3. The final rate of cutout of the intake line by the slide valve is proportional to the speed of the crankshaft. The energy losses are due to throttling of the flow in cross sections defined by the coverage of the valves in the slide valve, the "break" in the axial line of the intake tract, and the presence of breaks in the flow when it flows around sharp edges.

To estimate the loss, finite-difference expressions were used which were based on experimental and theoretical studies. In relation to the Reynolds number [2]

$$\Delta P_z = \left[\frac{A}{Re} + \left(1 - \frac{50}{Re} \right) \xi_{kv} \right] \left(\frac{Q}{F} \right)^2 \frac{\rho}{2},$$

where

$$A = 120 \left[\frac{1 + 0.5D_d (1 + \sin \delta)}{(1 - D_d^2 \sin \delta)^2} \right],$$

Re is the Reynolds number, D_d is the given diameter of the gate, δ is the angle of rotation of the gate, ξ_{kv} is a coefficient which considers the limit losses, ρ is the density of the medium, Q is the volume expenditure, and F is the cross sectional area.

Calculations have made it possible to establish the dependence of the throttle losses on the rate of closure of the cutout element (Figure 2, curves 3 and 4). Thus, the effect of the rate of the cutout of the intake line on filling is significant, from 4% to 10%.

Long before Volkswagen, the Scientific Research Automobile and Auto Motor Institute received an inventor's certificate on a means of using an effective degree of compression without the drawbacks which are characteristic of devices with a slide valve cutout mechanism [3]. In comparison to the latter, the device proposed by the Institute sharply reduces the work of the pumping strokes, decreases throttle losses, reduces flow through the closed cutoff device, reduces the volume between it and the main valve, and reduces the energy expenditures for the drive.

Conclusions

The use of an additional cutout device in the intake tract before the main intake valve for quantitative regulation of an internal combustion engine requires the following conditions: 1) a small gap in its contact with the casing; 2) the volume between the additional device and the intake valve should not exceed 10% of the cylinder volume; 3) the rate of closure of the cutout device should be shorter than the time for the crankshaft to rotate 40°.

BIBLIOGRAPHY

1. Ekspres-informatsiya "Porshnevyye i gazoturbinnyye dvigateli" [Express information "Piston and gas turbine engines"] 1988 No 24 pp 1-12.
2. Idelchik, I. Ye. Spravochnik po gidravlicheskim soprotivleniyam [Manual on hydraulic resistance] Moscow: Mashinostroyeniye 1975 360 pp.
3. A. s. 261026 SSSR. Mekhanizm izmeneniya effektivnoy stepeni szhatiya dvigatelya vnutrennego sgoraniya [Inventor's certificate 261026 USSR. Mechanism

to change the effective degree of compression of an internal combustion engine] N.
S. Khanin, B. N. Kapralov. BYULLETEN IZOBRETENIY 1970 No 4.

COPYRIGHT: "Izvestiya VUZov. Mashinostroyenie" 1990

UDC 532.526.4

Thermoanemometric Method of Measuring the Strength of Friction in Reverse Flows

907F0186b Moscow IZVESTIYA VYSSHIKH UCHEBNYKH ZAVEDENIY: MASHINOSTROYENIYE
in Russian No 1, Jan 90 pp 60-64

[Abstract and Article by Candidate of Technical Sciences G. A. Glebov, Candidate of Technical Sciences A. P. Kozlov, and Engineer A. A. Bormusov]

[Text]

ABSTRACT

This article describes the designs and principles of action of sensors and primary transformers for the measurement of the strength of friction on a wall in reverse flows with the direction of movement varying over time. The work of the examined measurement devices is based on the use of the thermoanemometer method to determine the instantaneous strength of friction and the use of the heat trace from the sensitive element of the thermoanemometer to determine the instantaneous strength of the action of the force of friction. Some results are presented of the testing of the method in a stalled flow before a ledge in a channel.

Complex turbulent flows with stalled zones are encountered in the flow tract of energy installations. A characteristic of these flows is the nonstationary position of the stall and junction points. Another characteristic is random, instantaneous reversal in the direction of movement of the flow in the vicinity of these points. Common methods of measuring the strength of friction in the wall using a floating element, Preston tubes, Stanton "deflectors", and Gardon type heat sensors [1] are not suited to the investigation of such flows. A pulse anemometer sensor is known [2] which can measure the average value of the strength of friction in a reverse flow. However, it has a very low frequency range and cannot measure instantaneous pulsations in friction, the frequency of the change in the direction of movement, and other characteristics.

Below, two thermoanemometric methods are described for the measurement of the strength of friction in reverse flows. In the first method, a sensor is used with three parallel thin threads located in one plane at a distance $H = 0.05-0.3$ mm from the surface of the wall. The central thread 1 (Figure 1) of the sensor is the sensitive element of the thermoanemometer, and determines the instantaneous value of the strength of friction at the wall

$$\tau = \mu(\partial u / \partial y)_{y=0} \approx \mu u_H / H, \quad (1)$$

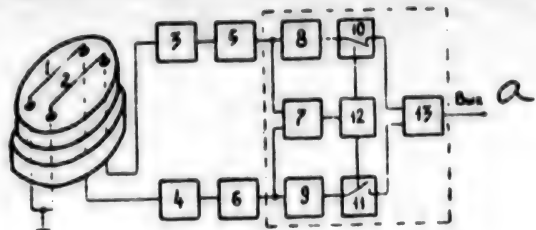


Figure 1. Schematic of the three-thread sensor and primary transformer. a. out.

where μ is the dynamic viscosity, and u is the speed of the flow at distance H from the wall. Two other lateral threads, 2 and 3, of the sensor are thermometers of resistance. Their purpose is to determine the instantaneous direction of movement of the flow, or the instantaneous direction of action of the force of friction along the heat trace from the heated thread of the thermoanemometer. These threads are 2.5-5.0 μm in diameter in fine holders 0.2 mm in diameter 4 located at 0.2-0.4 mm from the central thread on both sides.

In the first method, a standard thermoanemometer 5, linearizer 6 and correcting adapter are used as primary transformers to measure friction. The adapter consists of a differential amplifier 7, comparator 8, electronic switch 9, and an inverter-repeater 10. The input of the differential amplifier is connected with the diagonal of the resistive bridge. Resistance thermometers 2 and 3 are connected at the bridge's shoulder.

When thread 1 is not heated, the bridge is balanced. When the thread is heated, its heat trace, depending on the direction of the flow, falls on one of the thermal resistances. This creates either a positive or negative voltage which unbalances the bridge. This voltage is amplified by the differential amplifier and enters the comparator, which has a zero response threshold. The comparator forms signals to control the electronic switch of the inverter-repeater. At the input of the inverter-repeater the linearized output signal of the thermoanemometer enters. This signal is proportional to the instantaneous value of the strength of friction at the wall. Depending on the direction of the flow the inverter-repeater either inverts or repeats the phase of the input signal. Thus, a correlation is established between the output signal of the thermoanemometer and the instantaneous value of the strength of friction at the wall considering the direction of movement of the flow.

The other method uses a two-thread sensor. Each of the threads is the sensitive element of the thermoanemometer. The structure and size of the two-thread sensor is approximately the same as the three-thread model. Threads 1 and 2 (Figure 2) are parallel and 0.1-0.4 mm apart from each other. The primary transformer is two thermoanemometers 3 and 4 with linearization units 5 and 6 and a correcting adapter. The adapter consists of a differential amplifier 7, a matching cascade 8, an inverter 9, two electronic switches 10 and 11, a comparator 12, and summer 13. The instantaneous direction of movement of the flow is determined from the difference of the readings of thermoanemometers 3 and 4. The thermoanemometer in which the sensitive element-thread is in the heat trace reduces the output signal. The instantaneous strength of friction is determined by the same thermoanemometer whose sensitive element is not in the heat trace or is first in the flow.

Let us briefly describe the working principles of the correcting adapter (Figure 2). The linearized signals of thermoanemometers 3 and 4 enter differential amplifier 7,

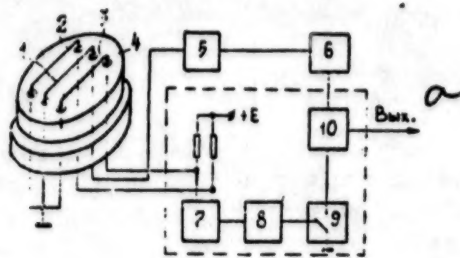


Figure 2. Schematic of the two-thread sensor and primary transformer. a. out.

which compares the input signals and controls comparator 12. The comparator forms signals for the control of switches 10 and 11. Depending on the direction of movement of the flow, switch 10 is opened and the signal of thermoanemometer 3 passes to the output of the device, or switch 11 is opened and the inverted signal of thermoanemometer 4 passes to the output.

The electrical schematics of the correcting adapters which determine the instantaneous direction of movement of the flow in the two methods examined are presented in [3]. We implemented these adapters in the form of instruments and tested them together with sensors for their working capacity. The standard thermoanemometers used were equipment of the DISA-55M system, which made it possible to make measurements of instantaneous flow speed with a pulsation frequency of up to 50 kHz.

The testing showed that the three-thread sensor makes it possible to record with high accuracy changes in the direction of movement of the flow in the opposite direction with a frequency of up to 100 Hz. The lateral threads have a slight effect on the reading of the central thread of the thermoanemometer. The probability of a possible failure of the thermal trace to fall on the lateral thread for the described sensor construction, even directly in the vicinities of the stall and junction points of the flow, did not exceed 1%, which has virtually no effect on the results of the measurements. The testing of the two-thread sensor showed a larger range of frequencies of flow reversal, up to 500 Hz. This increase in the frequency range, in comparison to the three-thread sensor, is explained by the fact that in that method both threads operate in constant temperature mode. The studies of many types of subsonic stalled flows that we performed showed that the frequency of reversal of flow does not exceed 40-70 Hz.

Testing of the described sensor structures also showed that the sensors must be friction graded. There are a number of problems associated with determining friction directly from formula (1). First, in manufacturing of the sensor it was difficult to maintain the identical distance H along the entire thread length. Second, one had to consider the effect of the closeness of the wall on the reading of the thermoanemometer. Another means of determining the strength of friction at the wall is with direct friction grading in a common boundary layer on film, which is, in our opinion, less labor-intensive and more reliable.

It should also be noted that in friction sensors, instead of threads one may use metal films applied to a special substrate. The use of films makes it possible to exclude the disturbing effect of the sensitive elements of the sensor on the flow.

Let us present several results of the study of flow in the region of a flow stall

before a ledge. These results were obtained using a three-thread friction sensor. The experiments were done in a subsonic aerodynamic tube which operated in exhaust mode. The working part of the tube was a rectangular channel 140 mm high and 360 mm wide. The ledge was 42 mm high and was located across the full width of the lower wall of the channel. The speed of flow before the ledge was regulated from 5 to 36 m/s. The collection and processing of information during the experiments was done using a measurement-computing complex based on a SM-4 computer using the Turbulence automated measurement system [4].

As a result of the processing of experimental results data were obtained on the average and pulsation components of the strength of friction τ , the alternation γ , and the frequency F of change in the direction of movement of the flow over time. The alternation was determined as a portion of time, during which the direction of movement of the medium at the measurement point coincided with the direction of movement of the external flow.

Figure 3 shows the schematic of flow and some results of the measurements of characteristics of flow in the stall region before the ledge. Analysis of the results of measurements showed that two flow modes were possible before the ledge: with the generation of a small recirculation zone before the stall region and without it. In the first case the friction at the wall changes sign four times, and in the second, two times. The maximum value of the average strength of friction at the wall is

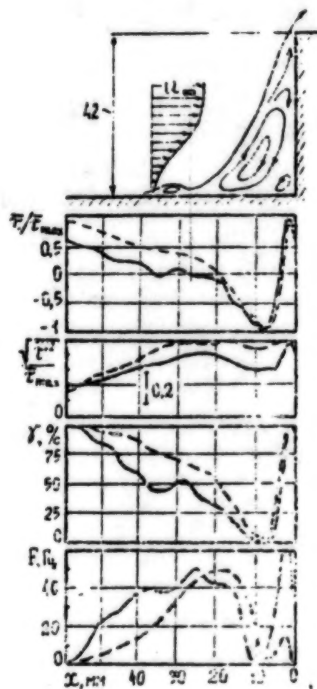


Figure 3. Structure of the flow in the region of flow stall before the ledge. Solid line, $u_{\infty} = 15 \text{ m/s}$, $(\bar{u}'^2)^{1/2}/u_{\infty} \approx 0.013$; $(\bar{u}'^2)^{1/2}/u_{\infty} \approx 0.116$. Dashed line, $u_{\infty} = 15 \text{ m/s}$.

observed approximately at the midpoint between the stall point and the base of the ledge, and the maximum pulsations in friction $(\bar{\tau}'^2)^{1/2}$ in the region of the flow stall from the wall, where $\bar{\tau} = 0$. In the regions of stall and junction of the flow, where the average strength of friction at the wall was equal to zero, $\gamma \approx 50\%$, and F reached maximum values. This result indicates that the points of stall and junction of the flow may be determined from the alternation values and the frequency of change in direction of the movement of the flow. Friction grading of the sensors is not necessary to measure alternation and frequency.

Thus, the suggested methods significantly expand the region of use of thermoanemometry to measure the strength of friction in reverse flows.

BIBLIOGRAPHY

1. G. A. Glebov et al. Sensor to measure forces in a boundary layer at a wall. IZVESTIYA VUZOV. MASHINOSTROYENIYE 1987 No 9.
2. Vestfal et al. New sound to measure speed and strength of friction at a wall in the region of an unstable stall flow. TEORETICHESKIYE OSNOVY INZHENERNYKH RASCHETOV 1981 Vol 103 No 3.
3. G. A. Glebov et al. Modern methods and instruments to study highly turbulent flows OBRAZTSOVYYE I VYSOKOTOCHNYYE SREDSTVA IZMERENIY. OBZORNAYA INFORM. 1986 No 1.
4. A. F. Dregalin et al. Automated system for the study of stalled and highly turbulent flows. IZVESTIYA VUZOV. AVIATSIONNAYA TEKHNIKA 1987 No 1.

COPYRIGHT: "Izvestiya VUZov, Mashinostroyenie" 1990

- END -

END OF

FICHE

DATE FILMED

18 April 1990